The Astrophysical Journal, 765:90 (21pp), 2013 March 10 doi:10.1088/0004-637X/765/2/90

THERMAL ESCAPE IN THE HYDRODYNAMIC REGIME: RECONSIDERATION OF PARKER'S ISENTROPIC THEORY BASED ON RESULTS OF KINETIC SIMULATIONS

Alexey N. Volkov[1] and Robert E. Johnson[1,2]
[1] Department of Materials Science and Engineering, University of Virginia, Charlottesville, VA 22904-4745, USA
[2] Physics Department, New York University, New York, NY 10003-6621, USA
Received 2012 August 31; accepted 2013 January 3; published 2013 February 20

ABSTRACT

The one-dimensional steady-state problem of thermal escape from a single-component atmosphere of mon- and diatomic gases is studied in the hydrodynamic (blow-off) regime using the direct simulation Monte Carlo method for an evaporative-type condition at the lower boundary. The simulations are performed for various depths into an atmosphere, indicated by a Knudsen number, Kn_0, equal to the ratio of the mean free path of molecules to the radial position of the source surface, ranging from 10 to 10^{-5}, and for the range of the source Jeans parameter, λ_0, equal to the ratio of gravitational and thermal energies, specific to blow-off. The results of kinetic simulations are compared with the isentropic model (IM) and the Navier–Stokes model. It is shown that the IM can be simplified if formulated in terms of the local Mach number and Jeans parameter. The simulations predict that at $Kn_0 < \sim 10^{-3}$ the flow includes a near-surface non-equilibrium Knudsen layer, a zone where the flow can be well approximated by the IM, and a rarefied far field. The corresponding IM solutions, however, only approach Parker's critical solution as λ_0 approaches the upper limit for blow-off. The IM alone is not capable for predicting the flow and requires boundary conditions at the top of the Knudsen layer. For small Kn_0, the scaled escape rate and energy loss rate are found to be independent of λ_0. The simulation results can be scaled to any single-component atmosphere exhibiting blow-off if the external heating above the lower boundary is negligible, in particular, to sublimation-driven atmospheres of Kuiper belt objects.

Key word: planets and satellites: atmospheres

Online-only material: color figures

1. INTRODUCTION

The escape from a planetary atmosphere of molecules with thermal energies greater than the gravitational binding energy is referred to as thermal escape. Since the prediction of the escape rates by the thermal and non-thermal processes determines the long-term evolution of planetary atmospheres, it has long been a subject of interest in the aeronomy of planetary objects in our solar system (e.g., Johnson et al. 2008) and more recently of interest in understanding the evolution of extrasolar planets (e.g., Lammer et al. 2009). The particular feature that limits the modeling effort is that escape occurs in a rarefied region of an atmosphere, usually referred to as exosphere, where the gas flow is essentially non-equilibrium. In this region, continuum models break down so that molecular kinetic simulations are required to accurately predict the atmospheric flow structure and the escape rates (e.g., Lammer et al. 2008).

Two distinct regimes of thermal escape, namely, hydrodynamic or blow-off and Jeans-like or evaporative regimes, can take place in a planetary atmosphere depending on the Jeans parameter, the ratio of the gravitational binding energy to the thermal energy of a molecule (e.g., Johnson et al. 2008). We use the words hydrodynamic escape and blow-off interchangeably here, although some authors reserve the word hydrodynamic for cases in which continuum models are applicable up to the exobase (e.g., Tian 2009). Here we assume that the hydrodynamic escape regime occurs if the value of the Jeans parameter is sufficiently small, so that the total enthalpy of fluid particles is larger than the depth of the gravitational well and flow accelerates to supersonic velocities inside the continuum part of the atmosphere. In the Jeans-like regime, which occurs at large Jeans parameters, the flow remains truly subsonic up to the exobase and only the fraction of molecules in the tail of the velocity distribution function is lost to escape. Although these distinct regimes have been identified since pioneering works by Chamberlain (1963) and Parker (1963), the ranges of conditions specific to each regime have not been clearly understood. In particular, hydrodynamic escape has been assumed to occur if the Jeans parameter *at the exobase* is smaller than ~2 (e.g., Hunten 1982) or 1.5 (Öpik 1963; Lammer et al. 2008) and the transition from the hydrodynamic to Jeans-like regime occurs over a broad range of Jeans parameter. This gave rise to so-called slow hydrodynamic escape models (Krasnopolsky 1999) based on Parker's (1964a, 1964b) model for solar wind and intended for description of the atmospheric flow in an intermediate range of the Jeans parameter (e.g., Johnson et al. 2008). Recently, Volkov et al. (2011a, 2011b) showed that the latter is incorrect and the transition occurs over a narrow range of Jeans parameter, the boundaries of which depend on the number of degrees of freedom of gas molecules. For a monatomic gas in which there is no heating above the lowest altitude modeled, they found that the transition occurs when the Jeans parameter at that altitude, i.e., *at the source*, is in the range 2–3.

This paper focuses on the consideration of the thermally induced, hydrodynamic escape regime. In the solar system, such flows are characteristic for outflows from surfaces of objects with low gravity such as comet nuclei (Crifo et al. 2002; Tenishev et al. 2008), early terrestrial atmospheres (Watson et al. 1981; Zahnle & Kasting 1986; Hunten et al. 1987), and atmospheres of the Kuiper belt objects (KBOs; Stern & Trafton 2008; Levi & Podolak 2009, 2011). The aeronomy of the extrasolar planets, in principle, appears to provide large variety of hydrodynamically escaping outflows, since stellar radiation can induce a transition to blow-off even in atmospheres on massive Jupiter-type exoplanets. A transition to blow-off has been predicted in multiple calculations of the

atmospheric structures of the close-in exoplanets including hydrogen atmospheres of hot Jupiters (Tian et al. 2005; Muñoz 2007; Penz et al. 2008; Murray-Clay et al. 2009; Koskinen et al. 2012) and also supported by results of spectral measurements revealing the traces of heavy species in extended exoplanets' atmospheres (Vidal-Madjar et al. 2003, 2004; Linsky et al. 2010).

Parker (1960, 1963) developed a theory of hydrodynamic escape in a gravitational field based on the isentropic model (IM) in which enthalpy and entropy along gas streamlines are assumed to be constant. In his theory, the hydrodynamically escaping flow starts from a subsonic velocity that monotonically increases eventually becoming supersonic. He found that a spherically symmetric isentropic flow corresponds to a critical solution of the IM and is possible only in a polyatomic gas for a limited range of Jeans parameter and is not possible in a monatomic gas. One can argue then that there should be a qualitative difference between outflows of mon- and polyatomic gases in a gravitational field. It has also been argued that the conditions of existence of Parker's critical solution allow one to constrain unknown conditions at the surface of a planetary body exhibiting a hydrodynamically escaping outflow (e.g., Levi & Podolak 2009).

Although Parker's IM of the hydrodynamics escape is simple and attractive, it does not appear to have been verified by kinetic simulations of flow in a gravity field. In this paper, we therefore attempt to verify assumptions of Parker's theory using the direct simulation Monte Carlo method (DSMC) and to compare predictions based on the kinetic model, IM, and full Navier–Stokes equations. Our simulations are performed over a broad range of Knudsen numbers, the ratio of the mean free path of gas molecules to the linear flow scale, covering the whole range of flow conditions from continuum flows in planetary atmospheres to almost free molecular outflows that are relevant to collisionless atmospheres of certain asteroids (Schläppi et al. 2008).

Our main finding is that the flows of mon- and diatomic gases found in kinetic simulations are similar, contrary to expectations based on Parker's theory. At small Knudsen numbers at the source, our DSMC simulations show that the flow of both mon- and diatomic gases in the hydrodynamic escape regime always contains a zone in which the flow structure can be well approximated by the IM, but the corresponding solution of the IM does not coincide with Parker's critical solution. This disagreement with Parker's theory is explained by the formation of a non-equilibrium Knudsen layer at the source surface. In order to apply either the IM or full Navier–Stokes equations for the flow in that zone, one must know the parameters at the top of the Knudsen layer, and thus the IM *alone* is not able to correctly predict the structure of hydrodynamically escaping flows. The parameters at the lower boundary of the isentropic flow zone can be provided by calculations based on kinetic models. These parameters, including number and energy escape rates, are obtained for the whole range of relevant Knudsen numbers and Jeans parameters. It is also shown that the analysis of the IM is significantly simplified if carried out in terms of the local Mach number and Jeans parameter, an approach that appears not to have been used in any previous study.

Since we do not consider atmospheric heating processes, the results obtained in the present paper can be applied only to upper parts of atmospheres, where heating by the stellar radiation or the ambient plasma is either negligible or a small fraction of the net upper atmospheric heating rate. This has been approximated in the past by introducing the concept of an infinitely thin heated layer (Watson et al. 1981), although the applicability of this approach for hot Jupiters is questionable (Tian et al. 2005). We believe, however, that the study of the general properties of blow-off undertaken in the present paper results in the better understanding of the limitations of Parker's model, which is mentioned in virtually every paper on the aeronomy of close-in exoplanets.

The results of our simulations, on the other hand, can be directly applied to the atmospheres of icy bodies populating, for example, the Kuiper belt of the solar system. For instance, for medium-sized KBOs with radii R_0 below ~200 km and surface temperatures ~30 K estimated from radiative equilibrium at heliocentric distances of 50 AU, the most volatile species such as N_2, CO, and CH_4 have the source Jeans parameter smaller than 2 (Stern & Trafton 2008), which is below the critical Jeans parameter for transition to Jeans-like escape found by Volkov et al. (2011a, 2011b). For these conditions, the surface vapor pressure varies from $\sim 10^{-8}$ Pa for CH_4 to $\sim 10^{-3}$ Pa for N_2 (Stern & Trafton 2008), which roughly corresponds to the mean free path of gas molecules l_0 ranging from 10^5 m to 1 m, or to the range of Knudsen number, $Kn_0 = l_0/R_0$, from 1 to 10^{-5}, which is fully considered in the present paper. The differences between our simulations and previous attempts to describe the KBO atmospheres based on Parker's theory (Levi & Podolak 2009, 2011) are highlighted in Section 3.

The presence of a non-equilibrium Knudsen layer at the surface of a body, evaporating into vacuum, of course, is a well-known feature for flows at zero gravity (see, e.g., Cercignani 2000; Davidsson 2008 and references therein). It is known to be important, for example, for near nucleus comet atmospheres, which is one of the reasons why studies of flows in comet atmospheres require kinetic simulations (Marov et al. 1996; Crifo et al. 2002; Tenishev et al. 2008). For comets, however, the effect of the gravitational field of a nucleus on the near nucleus coma is negligible so that the flow is often governed by the non-uniform thermal state over a rotating nucleus (Volkov & Lukyanov 2007) and non-homogeneous composition of the nucleus surface with distinct active zones (Combi et al. 2012). Here, we focus on conditions for which the gravity has a non-negligible effect on atmospheric blow-off. To the best of our knowledge, this is the first study reporting the results of the direct numerical calculations of the Knudsen layer in the presence of a gravitational field.

2. MODELS OF THE THERMAL ESCAPE

2.1. Kinetic Model of Thermal Escape

The kinetic model of flow in a spherically symmetric neutral atmosphere is described in detail elsewhere (Volkov et al. 2011b, 2013). In this section, therefore, only a brief description of the model is provided.

In a kinetic approach, the flow in a neutral planetary atmosphere is described in terms of a distribution function for the gas molecules. The set of arguments for this function depends on the adopted model of gas molecules and the flow symmetry. Assuming a continuous distribution of energy of molecules with internal degrees of freedom and one-dimensional, spherically symmetric flow of a single component, the distribution function $f(r, v_{||}, v_{\perp}, \varepsilon_i, t)$ depends on time t, radial distance from the planet center r, parallel $v_{||}$ and perpendicular $v_{\perp}$ components of molecular velocities, and energy of internal degrees of freedom of an individual molecule ε_i. Any gas parameter, including

number density n, gas velocity u, parallel $T_{||}$, perpendicular $T_{\perp}$, and total T temperatures, temperature of the internal degrees of freedom T_i, the number, Φ_n, and energy, Φ_e, escape rates can be considered as a functional of $f(r, v_{||}, v_{\perp}, \varepsilon_i, t)$ (Volkov et al. 2011b). In the kinetic theory, $f(r, v_{||}, v_{\perp}, \varepsilon_i, t)$ should satisfy a generalized Boltzmann equation (Ferziger & Kaper 1972). Instead of solving this equation, in this paper we perform simulations with the DSMC method (Bird 1994) in which the gas flow is represented by a large number of simulated molecules whose motion is subject to a gravitational field and binary collisions. This method is known to be a stochastic numerical method for estimation of the functionals of solutions of the Boltzmann kinetic equation (Wagner 1992).

In simulations, three models of gas molecules are considered: the hard sphere (HS) model of a monatomic gas, when molecules do not have internal degrees of freedom (number of internal degrees of freedom $\zeta = 0$) and their differential cross section is equal to $\sigma = d^2/4$ (d is the molecular diameter); the pseudo-Maxwellian (PM) model of a monatomic gas with the viscosity index $\omega = 1$ and $\zeta = 0$ in which collisions are described by the variable hard sphere model (Bird 1994) with differential cross section $\sigma = \sigma_{\rm ref} c_{\rm r,ref}/c_r$ (c_r is the relative velocity for a pair of colliding molecules and $\sigma_{\rm ref} c_{\rm r,ref}$ is the model parameter); and the combined pseudo-Maxwellian–Larsen–Borgnakke (PMLB2) model for a diatomic gas with two internal degrees of freedom ($\zeta = 2$), when the collision cross section is given by the PM model and the energy transfer between translational and rotational degrees of freedom is described by the Larsen–Borgnakke model (Borgnakke & Larsen 1975; Bird 1994). In the case of the PMLB2 model, the probability of inelastic collisions (inverse collision number; see Bird 1994) is assumed to be equal to 1.

In all simulations performed, with the exception those that are described in Section 4, it is assumed that at the lower boundary of the simulation region, the source surface, $r = R_0$, all molecules with $v_{||} > 0$ have a Maxwell–Boltzmann distribution with given number density n_0, zero net flow velocity $u_0 = 0$, and temperature T_0, so that (Hinshelwood 1940; Bird 1994) for $v_{\parallel} > 0$:

$$f(R_0, v_{||}, v_{\perp}, \varepsilon_i, t) = \tilde{f}_{0t}(v_{||}, v_{\perp}) \tilde{f}_{0i}(\varepsilon_i), \tag{1a}$$

where

$$\tilde{f}_{0t}(v_{||}, v_{\perp}) = \frac{n_0}{(2\pi k T_0/m)^{3/2}} \exp\left(-\frac{m\left(v_{||}^2 + v_{\perp}^2\right)}{2kT_0}\right), \tag{1b}$$

$$\tilde{f}_{0i}(\varepsilon_i) = \frac{\varepsilon_i^{\zeta/2-1}}{(kT_0)^{\zeta/2}\Gamma(\zeta/2)} \exp\left(-\frac{\varepsilon_i}{kT_0}\right), \tag{1c}$$

($\Gamma(x)$ is the gamma-function, k is the Boltzmann constant, and m is the mass of a molecule). Equations (1) are referred to as evaporative-type boundary conditions, since they resemble the Hertz–Knudsen model describing surface evaporation (Cercignani 2000), when molecules returning to this surface are assumed to be absorbed. The effects of the additional outflow and heat flux at the source surface are considered in Section 4, where Equation (1) are replaced by the velocity distribution in first approximation of the Chapman–Enskog theory (Chapman & Cowling 1970).

At the exit boundary, $r = R_1$, it is assumed that all molecules leaving the domain with hyperbolic trajectories (i.e., with $v_{||} > 0$ and $v > v_e(R_1)$, where $v_e(r) = \sqrt{2GM/r}$ is the escape velocity, M is the mass of the planetary body, G is the gravitational constant, and $v = \sqrt{v_{||}^2 + v_{\perp}^2}$), escape the atmosphere, while all others return into the domain without collisions, so that

$$\text{at } v_{||} < 0\text{: } f(R_1, v_{||}, v_{\perp}, \varepsilon_i, t) = \begin{cases} f(R_1, -v_{||}, v_{\perp}, \varepsilon_i, t), & v < v_e(R_1) \\ 0, & v \geqslant v_e(R_1) \end{cases}. \tag{2}$$

For a fixed model of intermolecular collisions, the kinetic problem in a reduced (non-dimensional) form contains two governing parameters. These can be chosen to be the Knudsen number $Kn_0 = l_0/R_0$ and Jeans parameter $\lambda_0 = R_0/H_0$ at the source surface, where l_0 is the mean free path of gas molecules in equilibrium at given n_0 and T_0 ($l_0 = (\sqrt{2}\pi d^2 n_0)^{-1}$ for the HS model; $l_0 = \sqrt{8kT_0/(\pi m)}/(4\pi\sigma_{\rm ref} c_{r,\rm ref} n_0)$ for the PM и PMLB2 models (Bird 1994) and $H_0 = kT_0 R_0^2/(GMm)$ is the atmospheric scale height calculated at the source surface assuming barometric distribution of gas density (e.g., Johnson et al. 2008). Since the present paper is intended to reveal the general properties of kinetic and hydrodynamic models, the computational results are given in their reduced form as functions of λ_0, Kn_0, and the dimensionless distance $\xi = r/R_0$. This allows one to scale the results to an atmosphere of any object with properties known at some physical surface or a "surface" in the atmosphere. Volkov et al. (2011a) found that hydrodynamic escape with the evaporative-type boundary conditions in Equation (1) takes place for $\lambda_0 \leqslant \lambda_{c1}$, where λ_{c1} depends on the number of internal degrees of freedom ζ or the ratio $\gamma = c_p/c_V = (5+\zeta)/(3+\zeta)$ of specific heats at constant pressure, $c_p = (5+\zeta)(k/m)$, and volume, $c_V = (3+\zeta)(k/m)$. The approximate boundary for the blow-off regime corresponds to (Volkov et al. 2013)

$$\lambda_c = \frac{\gamma}{2}\frac{\gamma+1}{\gamma-1}\frac{T_*}{T_0}, \tag{3}$$

where T_* is the temperature at the sonic surface found for $\lambda_0 = 0$ and $Kn_0 \to 0$. Equation (3) gives $\lambda_c = 2.14$ and $\lambda_c = 3.17$ for mon- and diatomic gases, while the DSMC simulations result in only slightly smaller limiting values for the blow-off range: $\lambda_{c1} = 2.1$ and $\lambda_{c1} = 2.8$ for mon- and diatomic gases. For a diatomic gas, the value of λ_{c1} predicted in the DSMC simulations coincides with the low limit of the Jeans parameter, $\lambda_0 = 2\gamma$, of the applicability domain of Parker's isentropic theory; see Equation (19b) below. In the present paper, the consideration of thermal escape is constrained by condition $\lambda_0 < \lambda_{c1}$.

In order to find a solution of the steady-state problem, a DSMC simulation was started with empty computational domain that eventually was filled by molecules moving upward across the surface at $r = R_0$ as described by the boundary condition given by Equation (1). The steady state was assumed to be reached when the number flux of gas molecules, $4\pi r^2 nu$, becomes constant (within the error 0.1%–1% depending on the simulation conditions) throughout the computational domain. The details of the numerical techniques, its implementation in the thermal escape problem, and discussion of the choice of numerical parameters, including the effect of the position of the exit boundary are given elsewhere (Volkov et al. 2011c, 2013).

2.2. Hydrodynamic Model of Thermal Escape

The continuum gas flow in an atmosphere of a planetary body can also be described using the full Navier–Stokes equations,

e.g., Sedov (1997). Although only steady-state solutions are of interest in this paper, it will be shown in Section 3.2 that the steady-state formulation of the Navier–Stokes equations is practically useless for simulating the blow-off, since its solution is very sensitive to variations of Φ_n and Φ_e. In order to understand this and to consider what boundary conditions are necessary, we start with time-dependent equations and consider the solution in the limit that $t \to \infty$. These equations can be written for a one-dimensional, spherically symmetric flow in a gravitational field without external heating as (see, e.g., Volkov et al. 2007)

$$\frac{\partial \rho}{\partial t} + \frac{\partial (\rho u)}{\partial r} + \frac{2}{r}\rho u = 0, \tag{4a}$$

$$\rho\left(\frac{\partial u}{\partial t} + u\frac{\partial u}{\partial r}\right) = -\frac{\partial p}{\partial r} + \frac{\partial \tau_{rr}}{\partial r} + \frac{2}{r}\frac{2\tau_{rr} - \tau_{\theta\theta} - \tau_{\varphi\varphi}}{2} - \frac{GM\rho}{r^2}, \tag{4b}$$

$$\rho\left(\frac{\partial e}{\partial t} + u\frac{\partial e}{\partial r}\right) = -\frac{\partial q}{\partial r} - (p - \tau_{rr})\frac{\partial u}{\partial r} - \frac{2}{r}\left[\left(p - \tau_{rr} + \frac{2\tau_{rr} - \tau_{\theta\theta} - \tau_{\varphi\varphi}}{2}\right)u + q\right], \tag{4c}$$

where $\rho = mn$, $p = \rho kT/m$, and $e = c_V T$ are the gas mass density, pressure, and internal energy per unit volume, $q = -\kappa \partial T/\partial r$ is the heat flux described by the Fourier law with thermal conductivity κ, and τ_{rr}, $\tau_{\theta\theta}$, and $\tau_{\varphi\varphi}$ are the diagonal components of Newton's viscous stress tensor written in spherical coordinates, $\tau_{rr} = (4/3)\mu(\partial u/\partial r - u/r)$, $2\tau_{rr} - \tau_{\theta\theta} - \tau_{\varphi\varphi} = 3\tau_{rr}$, and μ is the shear viscosity. In the framework of the Chapman–Enskog theory (Chapman & Cowling 1970), Equation (4) together with Fourier's heat flux and Newton's stress tensor can be thought of as a first-order solution of the Boltzmann equation for a region of atmospheric flow with small deviations from the local equilibrium and μ and κ are functions of gas temperature and parameters of individual molecules. In particular, for a monatomic gas, where collisions between molecules are described by either HS ($\omega = 1/2$) or PM ($\omega = 1$) model, μ and κ are given by power laws (Bird 1994): $\mu = \mu_{\rm ref}(T/T_{\rm ref})^{\omega}$ and $\kappa = (3/2)c_p\mu$, where $\mu_{\rm ref} = (5/16)m\sqrt{kT_{\rm ref}/(\pi m)}/d^2$ and $\mu_{\rm ref} = kT_{\rm ref}/(2\pi\sigma_{\rm ref}c_{r,{\rm ref}})$ for the HS and PM models correspondingly, and $T_{\rm ref}$ is a some reference temperature that is further assumed to be equal to the surface temperature T_0 in Equation (1).

Equations (4a) and (4c) can be integrated and reduced to the steady-state equations

$$m\Phi_n = 4\pi r^2 \rho u, \tag{5a}$$

$$\Phi_e = m\Phi_n\left(c_p T + \frac{u^2}{2} - \frac{GM}{r}\right) + 4\pi r^2(q - \tau_{rr}u), \tag{5b}$$

while the momentum equation (4b) reduces to

$$\rho u\frac{\partial u}{\partial r} = -\frac{\partial p}{\partial r} + \frac{\partial \tau_{rr}}{\partial r} + \frac{3\tau_{rr}}{r} - \frac{GM\rho}{r^2}. \tag{5c}$$

Equations (5a) and (5b) also represent the number and energy escape rates in the kinetic model if all parameters in the right-hand side of these equations are calculated according to their kinetic definitions (Volkov et al. 2011b). In order to solve Equation (5), one needs to impose five independent boundary conditions. In a typical atmospheric flow problem, however, it is often the case that only number density n_0 and temperature T_0 are known or can be estimated at the surface, so that boundary conditions are

$$\rho(R_0) = \rho_0 = mn_0, \;\; T(R_0) = T_0. \tag{6}$$

Three remaining undefined parameters can be the number, Φ_n, and energy, Φ_e, escape rates as recently discussed in describing escape from Pluto's atmosphere by Tucker et al. (2012) and the velocity gradient at the surface $(du/dr)_0$. Following Parker (1964a, 1964b), one can neglect the viscosity and consider the flow of an inviscid gas with non-zero thermal conductivity. Such a model, referred to as the reduced Navier–Stokes model, does not require knowledge of $(du/dr)_0$, and only Φ_n and Φ_e need to be specified.

One can obtain a solution to Equation (4) in the steady-state limit accounting for the fact that blow-off is advection-dominated, while the dissipative processes play only a secondary role. Therefore, boundary conditions can be chosen based on the analysis of characteristics for the corresponding Euler equations obtained from Equation (4) at $\mu, \kappa = 0$, when the number of boundary conditions at every boundary is determined by the direction of gas velocity u with respect to the boundary and by the value of u with respect the sound speed, $c = \sqrt{\gamma kT/m}$. According to the characteristics-based analysis, one needs to specify at a subsonic inflow boundary all flow parameters, ρ_0, u_0, and T_0, while at a supersonic outflow boundary no boundary conditions are necessary (e.g., Fletcher 1991). Thus, assuming that the outflow boundary at $r = R_1$ is chosen in the region of the supersonic flow, only one parameter, e.g., Φ_n, needs to be specified in addition to Equation (6) in order to find a steady-state solution to Equation (4).

A unique steady-state solution from Equation (4) in reduced units can be obtained by fixing γ, ω, λ_0, the Reynolds and Peclet numbers, $Re_0 = \rho_0\sqrt{kT_0/m}R_0/\mu_0$ and $Pe_0 = c_p\rho_0\sqrt{kT_0/m}R_0/\kappa_0$, and reduced escape rate $\bar{u}_0 = u_0/\sqrt{kT_0/m} = \Phi_n/(4\pi R_0^2 n_0\sqrt{kT_0/m})$. Parameters ω and λ_0 have their direct counterparts in the kinetic model of thermal escape, γ is directly related to ζ, while Re_0 and Pe_0 can be represented in terms of Kn_0 and $\bar{u}_0$, and $Pe_0 = Pr \cdot Re_0$, where $Pr = c_p\mu_0/\kappa_0$ is the Prandtl number. Thus, in the blow-off regime, the boundary conditions for the Navier–Stokes equations require that $\bar{u}_0$ is specified, while in the kinetic model it is obtained as a result of solving the problem. For a steady-state problem based on the full Navier–Stokes model in the form of Equation (5), $\bar{\Phi}_e = \Phi_e/(\Phi_n kT_0)$ and $(d\bar{u}/d\bar{r})_0 = (du/dr)_0/(\sqrt{kT_0/m}/R_0)$ should be specified additionally, while the reduced Navier–Stokes model does not require $(du/dr)_0$. It is also worth noting that actual values of surface parameters in the kinetic model, $\rho(R_0)$, $u(R_0)$, and $T(R_0)$, are different from the parameters ρ_0, $u_0 = 0$, and T_0 in Equation (1) since the non-equilibrium Knudsen layer is formed in kinetic simulations at the source surface. Thus, in order to compare the kinetic and continuum models with an *identical* boundary condition, one must solve the continuum models, e.g., with initial or boundary values of gas parameters that are found preliminary in corresponding kinetic simulations.

2.3. Isentropic Model for Hydrodynamic Escape

Based on Equation (5) we reformulate Parker's (1963) IM for outflows in a gravitational field in terms of local Mach

number, $Ma = u/\sqrt{\gamma kT/m}$, and local Jeans parameter, $\lambda = GMm/(kTr)$. We show that such a formulation has multiple advantages with respect to exploring solutions in terms of gas velocity and radial distance. The phase portraits of the IM on the plane $(Ma, 1/\lambda)$ will be then used for comparison with results of kinetic simulation in Section 3.2.

In a steady state, Equations (5a) and (5b) reduce to

$$\frac{d}{dr}\left(c_V \ln\frac{T}{\rho^{\gamma-1}}\right) = P_S, \tag{7}$$

$$\frac{d}{dr}\left(c_p T + \frac{u^2}{2} - \frac{GM}{r}\right) = P_H, \tag{8}$$

where

$$P_S = \frac{1}{T}\left[P_H - \frac{1}{\rho}\left(\frac{d\tau_{rr}}{dr} + \frac{3\tau_{rr}}{r}\right)\right], \tag{9a}$$

and

$$P_H = \frac{1}{m\Phi_n}\frac{d}{dr}\left[4\pi r^2(\tau_{rr}u - q)\right] \tag{9b}$$

are the entropy and enthalpy production terms due to viscous dissipation and thermal conductivity.

In the hydrodynamic escape regime, the effects of viscous dissipation and thermal conductivity are presumably small, so that the change of the gravitational energy with r in the left-hand side of Equation (8) is counterbalanced by the change of the enthalpy of fluid particles $c_pT + u^2/2$. One can then reduce Equations (7) and (8) to the equations of the IM, where $P_S = 0$ and $P_H = 0$, and, thus, the entropy and enthalpy are independent of r, i.e.,

$$\frac{T}{\rho^{\gamma-1}} = \frac{T_0}{\rho_0^{\gamma-1}}, \tag{10}$$

$$c_pT + \frac{u^2}{2} - \frac{GM}{r} = c_pT_0 + \frac{u_0^2}{2} - \frac{GM}{R_0}. \tag{11}$$

In this section, subscript "0" denotes the gas parameters at an arbitrary reference level $r = R_0$. The model given by Equations (5a), (10), and (11) is essentially the IM that was used by Parker (1963) for solar wind flows and then adopted by others for the thermal escape of neutral species (e.g., Johnson et al. 2008). Only three boundary conditions, ρ_0, u_0, and T_0 at $r = R_0$, are needed for the IM model.

Equations (5a) and (10) imply that all the flow parameters can be represented by power functions of a single "principal" flow parameter and r. For instance, in order to describe the flow in terms of the Mach number Ma and use it as a principal parameter, then density, velocity, and temperature can be represented as follows:

$$\frac{\rho}{\rho_0} = \left(\frac{Ma_0}{Ma}\right)^{2/(\gamma+1)}\xi^{-4/(\gamma+1)}, \tag{12a}$$

$$\frac{u}{u_0} = \left(\frac{Ma}{Ma_0}\right)^{2/(\gamma+1)}\xi^{-2\gamma/(\gamma+1)}, \tag{12b}$$

$$\frac{T}{T_0} = \left(\frac{Ma_0}{Ma}\right)^{2(\gamma-1)/(\gamma+1)}\xi^{-4(\gamma-1)/(\gamma+1)}, \tag{12c}$$

where $\xi = r/R_0$. By inserting Equation (12) into the differentiated Equation (11), one can find that

$$\frac{dMa}{d\xi} = \frac{Ma}{(1-Ma^2)\xi}\left(\lambda\frac{\gamma+1}{2\gamma} - 2 - (\gamma-1)Ma^2\right), \tag{13}$$

where the local Jeans parameter is defined as

$$\lambda = \lambda_0\left(\frac{Ma}{Ma_0}\right)^{2(\gamma-1)/(\gamma+1)}\xi^{-(5-3\gamma)/(\gamma+1)}. \tag{14}$$

In order to solve Equations (13) and (14), one must impose the initial condition $Ma_* = Ma(\xi_*)$ of the Cauchy problem and the initial value of the Jeans parameter $\lambda_* = \lambda(\xi_*)$ at some point $\xi = \xi_*$. The only solutions that cannot be found in that way are those solutions that go through the critical point C with $\xi = \xi_C$, where $Ma = 1$ and the numerator and denominator of the right-hand side of Equation (13) simultaneously become zero and, thus, $\lambda = \lambda_C = 2\gamma$. The position of the critical point ξ_C is not limited by Equation (13) and is defined by conditions at the reference point. In particular, for convenience one can choose the reference point $r = R_0$ to be coincident with the critical point, i.e., $\xi_C = 1$. Four branches of the critical solution converge at the critical point, namely, two subsonic branches ($Ma < 1$) and two supersonic branches ($Ma > 1$). The slopes of these branches at the critical point are given by the equation

$$\left.\frac{dMa}{d\xi}\right|_{\xi_C=1} = \pm\sqrt{\frac{3}{2}\left(\frac{5}{3} - \gamma\right)}. \tag{15}$$

In the case of a monatomic gas with $\gamma = 5/3$, Equation (15) reduces to $dMa/d\xi = 0$, every pair of sub- and supersonic branches degenerates into a single branch, and Equation (13) has no true critical point and critical solutions. In this case, however, we use the terms "critical point" and "critical solution" in order to denote limit critical point and solution found at $\gamma \to 5/3$. The sign of derivative $dMa/d\xi > 0$ does not change along each branch of the critical solution, so that at $\gamma < 5/3$ a pair of branches with $dMa/d\xi > 0$ form a critical solution that corresponds to a flow with the Mach number continuously increasing from infinitely small to infinitely large values. Thus, the inclusion of gravity results in a transonic, isentropic solution with $dMa/d\xi > 0$ in the flow with monotonically expanding cross section $A = 4\pi r^2$. By contrast, at zero gravity, as it is well known from nozzle flow studies, an isentropic flow with $dMa/d\xi > 0$ and $dA/d\xi > 0$ is possible only starting at $Ma \geqslant 1$ (Zucker & Biblarz 2002).

Since the initial Jeans parameter λ_0 can be chosen arbitrarily, an infinite number of solutions can pass through any point (Ma_0, ξ_0) on the plane (Ma, ξ). This remains true for any principal parameter considered as function of ξ. In particular, in the approach developed by Parker (1960, 1963), who analyzed the topology of solutions of the IM on the plane $(u/\sqrt{2kT_0/m}, \xi)$, an infinite number of solutions can intersect each other in any point of that plane. In this picture, the possible solutions appear to be overcomplicated (see Figure 2 below). There is a better way to analyze the topology of solutions of the IM given by Equations (13) and (14). Namely, one can reduce these equations to a differential form that does not include any parameters except initial conditions. This is readily seen since one can exclude ξ from Equation (13) using Equation (14). In order to find an equation providing a unique relationship between Ma and λ in a form that is independent of conditions at the reference surface, we differentiate Equation (14) and, using Equation (13), obtain a differential

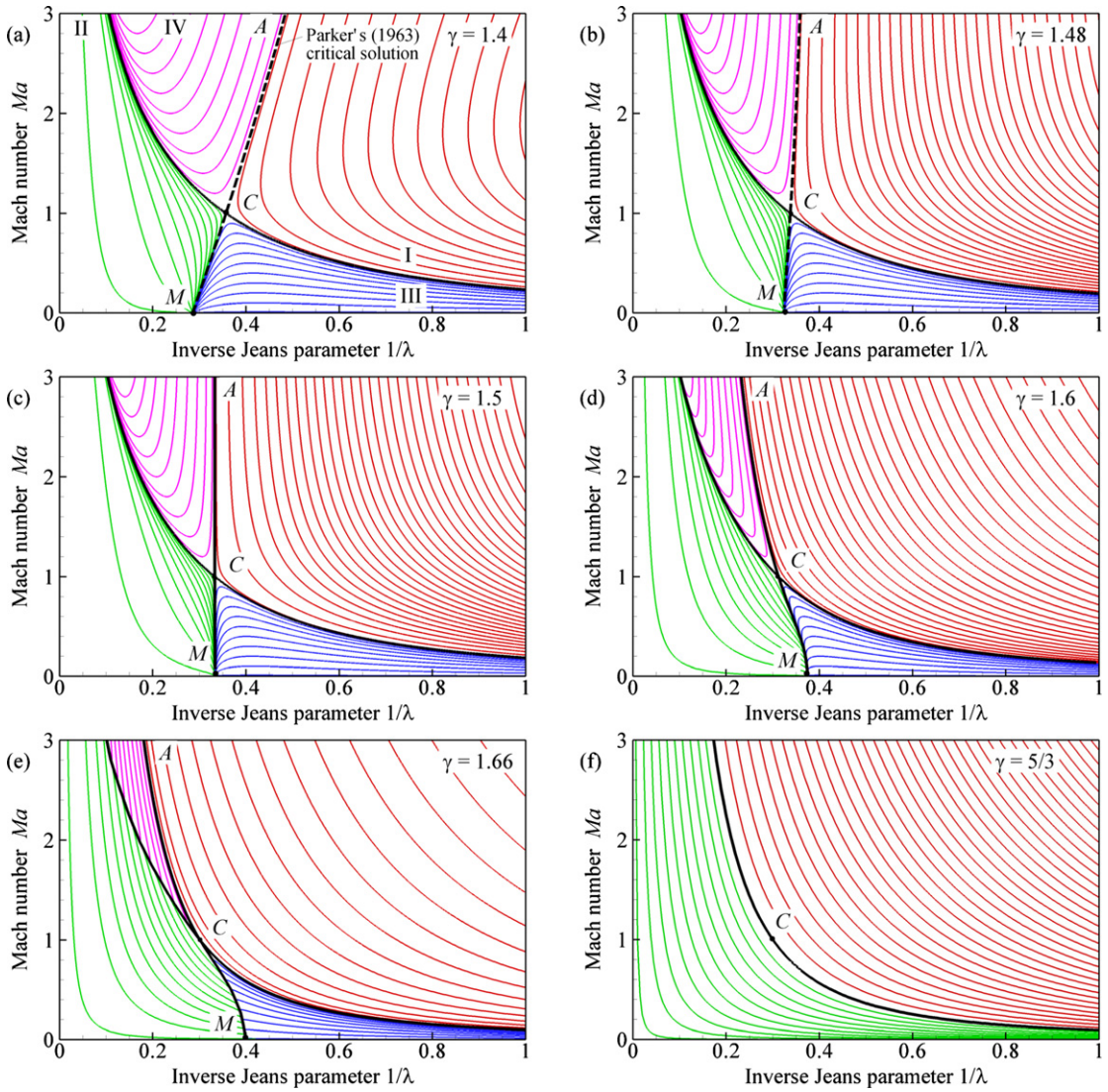

Figure 1. Phase portrait of the system given by Equation (17) at $\gamma = 1.4$ (a), $\gamma = 1.48$ (b), $\gamma = 1.5$ (c), $\gamma = 1.6$ (d), $\gamma = 1.66$ (e), and $\gamma = 5/3$ (f). At $\gamma < 5/3$, the phase portrait consists of four solution families (thin curves): I (red), II (green), III (blue), and IV (magenta), and critical solutions (thick solid and dashed curves, black) that go through the critical point C with $Ma_C = 1$ and $\lambda_C = 2\gamma$. At $\gamma = 5/3$ only solutions of families I and II exist that are divided by the single critical solution. In panel (f), point C marks the limit position of the critical point at $\gamma \to 5/3$. M marks the point with position $Ma_M = 0$ and $\lambda_M = \gamma/(\gamma - 1)$. MCA marks two branches of the critical solutions, where $dMa/d\xi > 0$. Thick dashed curves correspond to Parker's (1963) critical solution. Families of solutions shown in panels (a)–(e) are obtained by solving Equation (17), while solutions shown in panel (f) are obtained with Equation (18).

(A color version of this figure is available in the online journal.)

equation for λ

$$\frac{d\lambda}{d\xi} = \frac{\lambda}{(1 - Ma^2)\xi}\left(2\frac{\gamma - 1}{\gamma + 1}\left(\lambda\frac{\gamma + 1}{2\gamma} - 2 - (\gamma - 1)Ma^2\right) - \frac{5 - 3\gamma}{\gamma + 1}(1 - Ma^2)\right). \quad (16)$$

By dividing Equation (13) by Equation (16), we find a direct relationship between Ma and λ

$$\frac{dMa}{d\lambda} = \frac{Ma}{\lambda}\frac{\lambda\frac{\gamma+1}{2\gamma} - 2 - (\gamma - 1)Ma^2}{2\frac{\gamma-1}{\gamma+1}\left(\lambda\frac{\gamma+1}{2\gamma} - 2 - (\gamma - 1)Ma^2\right) - \frac{5-3\gamma}{\gamma+1}(1 - Ma^2)}. \quad (17)$$

The critical point corresponds to $Ma_C = 1$ and $\lambda_C = 2\gamma$ and coincides, of course, with the critical point for Equation (13). However, the critical point, or any initial point (Ma_0, λ_0), corresponds to a unique solution of the IM that is represented by a curve on the phase plane $(Ma, 1/\lambda)$ (Figure 1). These curves form a phase-plane portrait of the IM and do not intersect each other with exception of the critical solutions shown in Figure 1 by thick solid and dashed curves. These converge to the critical point C. For a monatomic gas ($\zeta = 0$) the general solution of Equation (17) can be obtained from Equation (14) using $\gamma = 5/3$:[3]

$$\frac{\lambda}{\lambda_0} = \sqrt{\frac{Ma}{Ma_0}}. \quad (18)$$

[3] Equation (17) can be also integrated in a limit case of a polyatomic gas with $\gamma = 1$ ($\zeta \to \infty$), when the solution becomes $\ln(Ma/Ma_0) - (Ma^2 - Ma_0^2) = \ln(\lambda/\lambda_0)^2 - (\lambda - \lambda_0)$. The case of $\gamma = 1$, corresponding to a near isothermal atmosphere, has been used to predict the flow in close-in exoplanet atmospheres (Stone & Proga 2009). We believe that a solution of Equation (17) for $\gamma = 1$ is not realistic, since in our model γ is the adiabatic index and, thus, is related to the activated degrees of freedom of gas molecules. The case $\gamma = 1$, therefore, is not considered in the present paper.

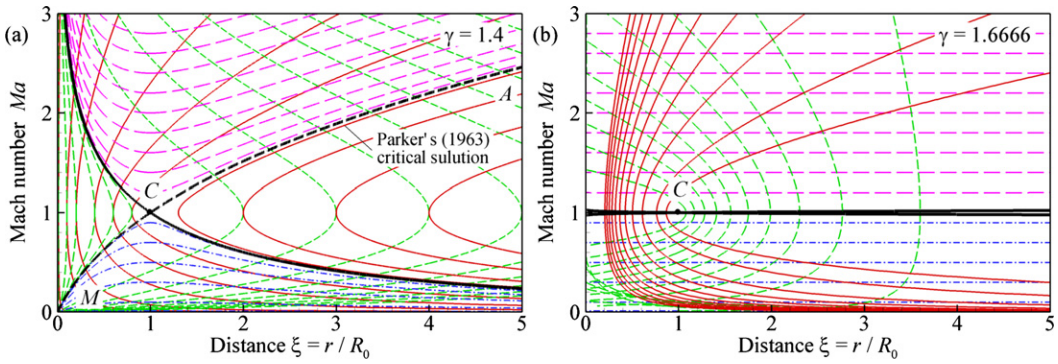

Figure 2. Typical solutions of Equation (13) at $\gamma = 1.4$ (a) and $\gamma = 1.6666$ (b). Thick solid and dashed curves (black) correspond to critical solutions with the critical point C at $\xi = 1$. Thin solid curves (red), dashed curves (green), dash-dotted curves (blue), and long-dashed curves (magenta) correspond to solutions of families I, II, III, and IV. In panel (a), solutions of family I are plotted for $\lambda_1 = 2\gamma$ at $\xi_1 > 1$ and $\lambda_1 = 2\gamma\xi_1^{2(5-3\gamma)/(\gamma+1)}$ at $\xi_1 < 1$, where λ_1 and ξ_1 are imposed values of λ and ξ at $Ma = 1$; solutions of family II are plotted for $\lambda_1 = 2\gamma\xi_1^{2(5-3\gamma)/(\gamma+1)}$ at $\xi_1 > 1$ and $\lambda_1 = 2\gamma$ at $\xi_1 < 1$. In panel (b), solutions of families I and II are plotted for $\lambda_1 = 2\gamma$. Solutions of families III and IV in both panels (a) and (b) are plotted for $\lambda_1 = 2\gamma[2 + (\gamma - 1)Ma_1^2]/(\gamma + 1)$, where λ_1 and Ma_1 are imposed values of λ and Ma at $\xi = 1$. In panel (a), thick dashed curve MCA shows Parker's (1963) critical solution. At arbitrary γ, only solutions of family I have a supersonic part with $dMa/d\xi > 0$.

(A color version of this figure is available in the online journal.)

As one can see from Figure 1, at $\gamma < 5/3$, the IM has four solution families divided by branches of the critical solution: family I, where both Ma and λ can be arbitrary; family II, where Ma is arbitrary, but λ is limited by the condition $\lambda > \lambda_C = 2\gamma$ at $\gamma < 3/2$ or by the condition $\lambda > \lambda_M = \gamma/(\gamma - 1)$ at $\gamma > 3/2$; subsonic family III, and supersonic family IV. Examples of solutions of various families in the form of $Ma(\xi)$ are shown in Figure 2(a) by curves of different colors that correspond to the color of the solution families in Figure 1(a). At the sonic point ($Ma = 1$), any solution of families I and II has $d\xi/dMa = 0$, while the sign of the second derivative is different for families I and II. The solutions of family I at the sonic point have $\lambda < 2\gamma$ and $d^2\xi/dMa^2 > 0$, so that such solutions achieve their minimum at the sonic point and their supersonic branches propagate to infinitely large ξ having $dMa/d\xi > 0$. The solutions of family II at the sonic point have $\lambda > 2\gamma$ and $d^2\xi/dMa^2 < 0$. Such solutions achieve their maximum ξ at the sonic point and their supersonic branches have $dMa/d\xi < 0$. Thus, any isentropic flow with initial conditions (Ma_0, λ_0) within the region of solutions of family II cannot be continued up to an infinite ξ.

Parker (1960, 1963) analyzed the IM for solar wind flows in terms of u as a function of r. He considered the solutions that start with small u at the source surface and then proceed with $du/dr > 0$ to very high velocities at large r. In that way, he found that the continuous acceleration of the flow from small to large u is possible only if the flow first follows the critical solution given by the curve MC in Figure 1(a) and then proceeds along the upper branch of the critical solution given by curve CA in Figure 1(a). This conclusion was subsequently confirmed by Carovillano & King (1965), who used a different approach for analyzing the IM. The condition $du/dr > 0$ is satisfied along MC and CA only for polyatomic gases with $\gamma < 3/2$. Since $\lambda_C < \lambda < \lambda_M = \gamma/(\gamma - 1)$ for such γ Parker finally concluded that the physically realized flow, which starts at a reference surface with a subsonic velocity, should follow the critical solution of the IM and must satisfy the following conditions:

$$\gamma < 3/2, \tag{19a}$$

$$2\gamma < \lambda_0 < \frac{\gamma}{\gamma - 1}. \tag{19b}$$

Since these conditions are not satisfied for a monatomic gas, one can argue that spherically symmetric hydrodynamically escaping flows of a monatomic gas should be different from flows of polyatomic gases (Parker 1963; Levi & Podolak 2009).

Our analysis of isentropic flow is in agreement with Parker's analysis: Although the transonic critical solution with $dMa/d\xi > 0$ always exists at $\gamma < 5/3$, the subsonic branch of this solution satisfies the condition $du/dr > 0$ only at $\gamma < 3/2$. In Section 3, we will show that Parker's assumption that all physically realized flows must have $du/dr > 0$ is, in fact, incorrect. On the other hand, we show below that $dMa/d\xi > 0$ is found to be satisfied in all flows considered in our kinetic simulations in both mon- and diatomic gases.

3. RESULTS OF KINETIC SIMULATIONS OF HYDRODYNAMIC ESCAPE WITH EVAPORATIVE-TYPE BOUNDARY CONDITIONS

3.1. Comparison of Flow Structures in Mon- and Diatomic Gases

Distributions of gas parameters found in the DSMC simulations in the regime of hydrodynamics escape are shown in Figures 3–5 for mon- and diatomic gases. At small Kn_0, at the source surface, a Knudsen layer is formed, where the flow transforms from a non-equilibrium flow near the source to near equilibrium at the top boundary of this layer, as discussed earlier by Volkov et al. (2011a, 2011b). Since the flow in the Knudsen layer is non-equilibrium and, hence, non-isentropic, both enthalpy $h = c_pT + u^2/2 - GM/r$ and entropy $s = c_V \ln(T/\rho^{\gamma-1})$ vary across this layer (Figures 3(a) and (b)). Outside the Knudsen layer, h and s tend to be constant at small Kn_0 up to fairly large distances from the source (Figures 3(c) and (d)). This indicates that a hydrodynamically escaping flow for $\lambda_0 > 0$ can be approximated outside the Knudsen layer by the IM, as discussed in the next section.

The typical thickness of the Knudsen layer, δ_K, is a few tens of mean free paths of gas molecules at the source surface, l_0, and, thus, δ_K/R_0 tends to zero as Kn_0 decreases. The changes in the gas parameters across the Knudsen layer, however, remain finite even in the limit $Kn_0 \to 0$, as suggested by simulations with small $Kn_0 = 10^{-4} - 10^{-5}$. Therefore, the parameters at the

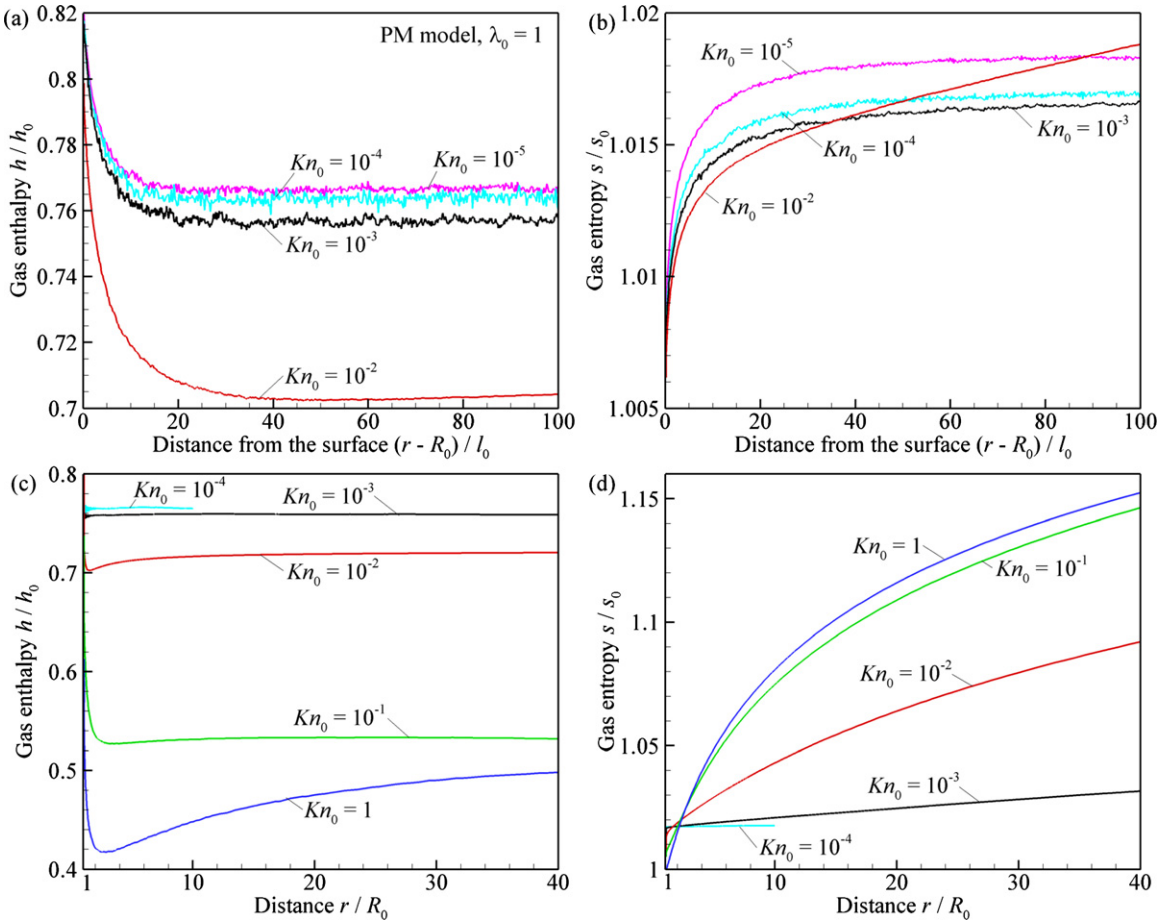

Figure 3. Distributions of gas enthalpy h/h_0 (panels (a) and (c)) and entropy s/s_0 (panels (b) and (d)) vs. distance from the source surface $(r - R_0)/l_0$ (panels (a) and (b)) and distance from the source center r/R_0 (panels (c) and (d)) found in kinetic simulations with the PM model ($\gamma = 5/3$, $\omega = 1$) at $\lambda_0 = 1$ and various Kn_0. Curves are marked with $Kn_0 = 10^{-5}$ (magenta), $Kn_0 = 10^{-4}$ (cyan), $Kn_0 = 10^{-3}$ (black), $Kn_0 = 10^{-2}$ (red), $Kn_0 = 10^{-1}$ (green), and $Kn_0 = 1$ (blue).
(A color version of this figure is available in the online journal.)

top of the Knudsen layer differ from the surface parameters even when $Kn_0 \to 0$. Distributions shown in Figure 4 clearly reveal an absolute convergence of the flow structure with decreasing $Kn_0 \to 0$ to some limit, where it becomes independent of Kn_0 at large distances from the source. This limit can be described by the IM. At any finite Kn_0, the isentropic flow zone gradually gives way to the far field, the zone of non-equilibrium transitional and near free molecular flow, where the lack of collisions results in the deviation between parallel and perpendicular temperatures (Figure 6). In particular, the perpendicular temperature drops to zero, while the parallel temperature goes to a non-zero asymptotic value that results in finite terminal Mach numbers. This qualitative picture of a spherical outflow in the far field at zero gravity is known since pioneering work by Hamel & Willis (1966) and Edwards & Cheng (1966) and has been recently confirmed by Volkov et al. (2011b) for flows at non-zero gravity. It is worth noting that there is a strong change in h and s as Kn_0 drops from 10^{-2} to 10^{-3}. This is an indication that a true Knudsen layer, above which there is an isentropic flow zone, is formed only at $Kn_0 < \sim 10^{-3} - 3 \times 10^{-3}$. At $Kn_0 > 10^{-2}$, the flow remains non-equilibrium throughout; at $Kn_0 \geqslant 1$ the flow can be fairly well approximated by the free molecular flow model (Öpik & Singer 1961; Lemaire 1966). That free molecular flow deviates significantly from the predictions based on the IM (Volkov et al. 2011b). The condition $Kn_0 < \sim 10^{-3} - 10^{-2}$ defines the lower limit of surface vapor pressure and, thus, the surface temperature, when the IM can be applicable for the description of rarefied KBO atmospheres (Levi & Podolak 2009).

Distributions of the Mach number, temperatures, and many other parameters for mon- and diatomic gases exhibit a similar behavior as shown by Volkov et al. (2013). Here, therefore, we compare only the distributions of velocity and local Jeans parameter for mon- and diatomic gases (Figure 5) in order to reveal the following minor qualitative differences between flows of these gases and in the blow-off regime.

First, in the diatomic gas the velocity is always an increasing function of r/R_0, while for a monatomic gas a non-monotonic dependence is found (Figures 4(a), 5(a), and (b)). The height of the maximum in the gas velocity (with respect to the terminal velocity) rises with increasing λ_0. This clearly shows that the hypothesis, $du/dr > 0$, that Parker (1963) used for selection of physically realized solution of the IM is incorrect for a monatomic gas. The local Mach number, on the other hand, is found to be a monotonically increasing function of r/R_0 in all simulation performed (e.g., Figure 4(b)).

Second, in both gases at small Kn_0, the gas temperature T can fall faster than $1/r$ (Figure 4(c)), so that the local Jeans parameter is not a monotonic function of r/R_0 (Figure 4(d)). In a diatomic gas, however, the thickness of the region, where T drops faster than $1/r$ is very narrow and attached to the Knudsen layer. By contrast, in a monatomic gas T drops faster than $1/r$

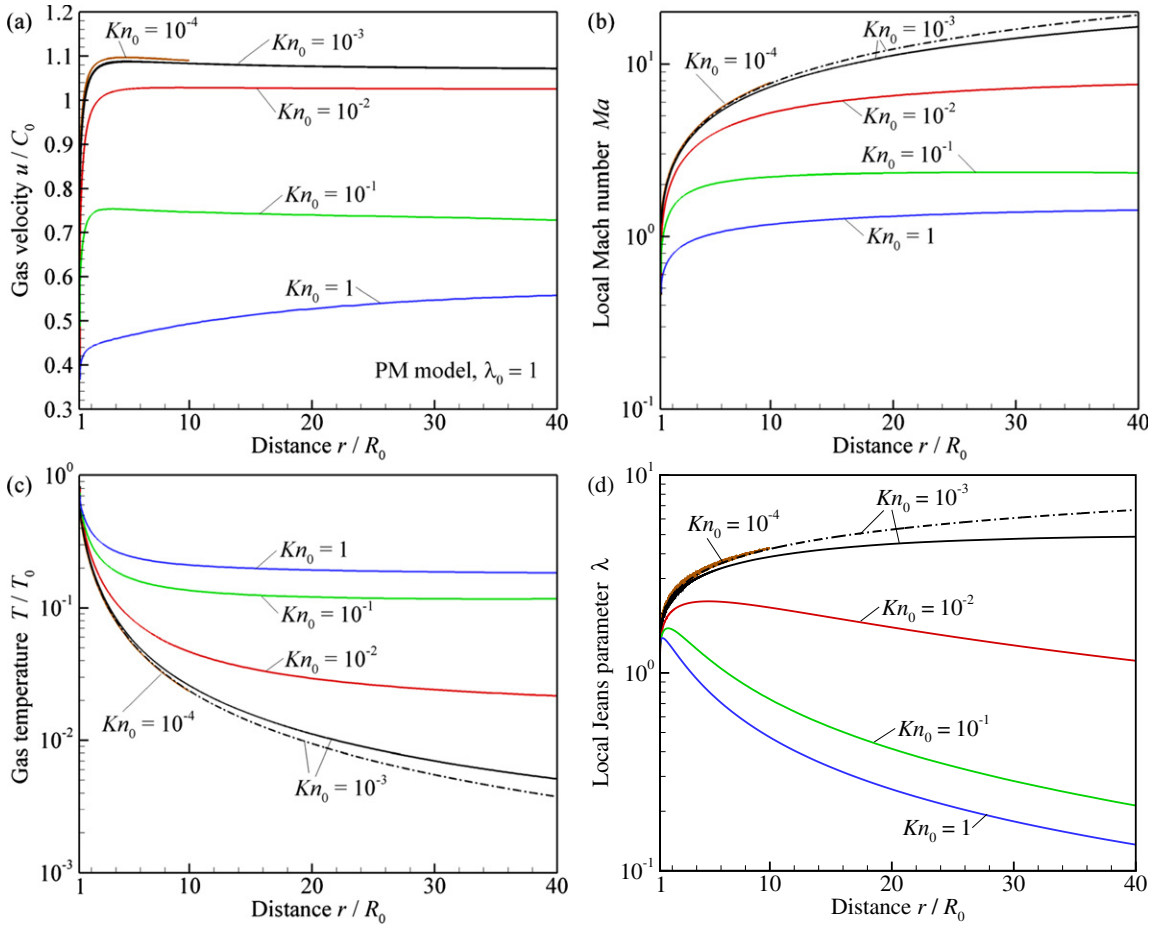

Figure 4. Distributions of gas velocity u/C_0 (a), local Mach number $Ma = u/\sqrt{\gamma kT/m}$ (b), temperature T/T_0 (c), and local Jeans parameter $\lambda = GMm/(kTr)$ (d) vs. distance r/R_0 found in kinetic simulations with the PM model ($\gamma = 5/3$, $\omega = 1$) at $\lambda_0 = 1$ and various Kn_0. Curves are marked with $Kn_0 = 10^{-4}$ (brown), $Kn_0 = 10^{-3}$ (black), $Kn_0 = 10^{-2}$ (red), $Kn_0 = 10^{-1}$ (green), and $Kn_0 = 1$ (blue). Dash-dotted curves are calculated with the IM with onset at the top boundary of the Knudsen layer, $r = r_K$, where r_K is given by Equation (20) and using initial parameters found in the DSMC simulations at $Kn_0 = 10^{-3}$. In panel (a), the dash-dotted curve visually coincides with solid curve for $Kn_0 = 10^{-3}$. Flow field at $Kn_0 = 10^{-4}$ was calculated with $R_1/R_0 = 10$. $C_0 = \sqrt{2kT_0/m}$.
(A color version of this figure is available in the online journal.)

up to fairly large distances from the source. As a result, in a diatomic gas the region with $d\lambda/d\xi > 0$ is narrow, while in a monatomic gas $d\lambda/d\xi$ remains positive up to the upper boundary of our computational domain.

3.2. Comparison of Results of Kinetic Simulations with the Isentropic Model

At $Kn_0 < \sim 10^{-3} - 3 \times 10^{-3}$, the distributions of gas parameters found in the DSMC simulations for both mon- and diatomic gases agree fairly well with the distributions predicted by the IM outside the Knudsen layer (dash-dotted curves in Figures 4 and 5) and demonstrate qualitative features that were previously established based on the analysis of the IM. First, for both mon- and diatomic gases, the local Mach number is an increasing function of distance for all r. Second, for a monatomic gas, velocity u can be a decreasing function of distance. Finally, in a monatomic gas, the fast drop in temperature and rise in local Jeans parameter agree with Equation (18).

The degree of deviation of the kinetic solution from the solution of the IM is different for different parameters. The deviation in temperature increases relatively fast with r due to increasing difference between parallel and perpendicular temperatures and the same is true for other temperature-dependent parameters such as Ma and λ. On the other hand, densities and velocities found in the DSMC simulations and calculated with the IM remain close to each other to very large distances from the source. In particular, at $Kn_0 = 10^{-3}$ the difference in u remains of the order of a few percent up to the external boundary of our computational domain, $R_1/R_0 = 40$. Thus, at $Kn_0 \leqslant 10^{-3}$, the IM predicts the flow at fairly large distances from the source with accuracy sufficient for atmospheric studies.

In order to show how the flow structures found in the DSMC simulations for both mon- and diatomic gases correlate with the critical solutions of the IM, the distributions of gas parameters found in the DSMC simulations at $Kn_0 = 10^{-3}$ were recalculated in the form of curves $f(Ma, \lambda) = 0$, which were plotted on top of the phase portraits of the IM in Figure 7. The lowest points of the thick curves representing the DSMC solutions in Figure 7 correspond to the source surface. It is seen that in both gases a DSMC solution found at a small Knudsen number can be divided into two distinct parts. The first, which corresponds to the near surface Knudsen layer, crosses individual solutions of the IM, since in the Knudsen layer $h, s \neq$ const. At sufficiently large λ_0, this part of the DSMC solution can intersect one branch of the critical solution. The second part closely follows an individual solution of the IM. The supersonic part of the DSMC solution lies in the region of solutions of family I of the IM. It is surprising that at $\lambda_0 < 2$ for both mon- and diatomic gases, the flow does not follow

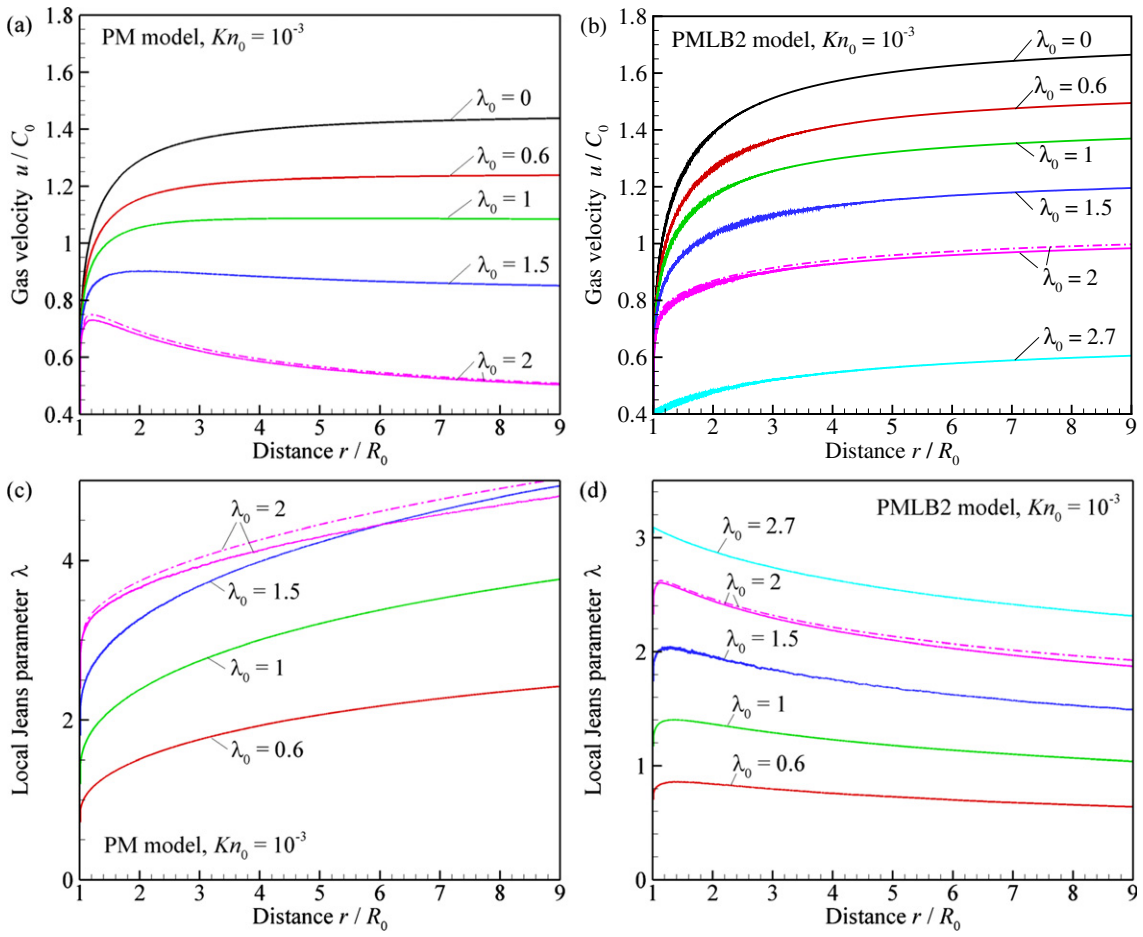

Figure 5. Distributions of gas velocity u/C_0 (panels (a) and (b)) and local Jeans parameter $\lambda = GMm/(kTr)$ (panels (c) and (d)) vs. distance r/R_0 found in kinetic simulations with for monatomic gas (PM model, panels (a) and (c)) and diatomic gas (PMLB2 model, panels (b) and (d)) at $Kn_0 = 10^{-3}$ and various λ_0: $\lambda_0 = 0$ (black), $\lambda_0 = 0.6$ (red), $\lambda_0 = 1$ (green), $\lambda_0 = 1.5$ (blue), $\lambda_0 = 2$ (magenta), and $\lambda_0 = 2.7$ (cyan). Dash-dotted curves are calculated with the IM and parameters at the sonic surface found in the DSMC simulations at $\lambda_0 = 2$. $C_0 = \sqrt{2kT_0/m}$.

(A color version of this figure is available in the online journal.)

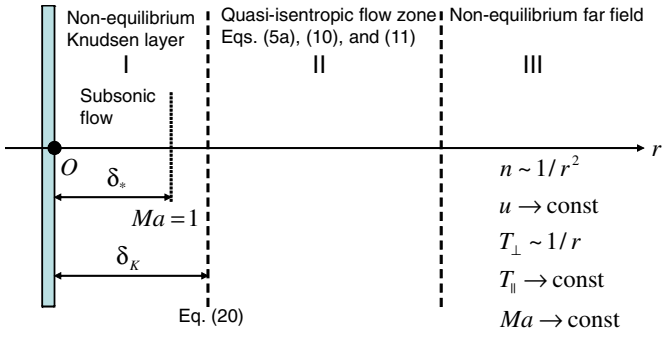

Figure 6. Schematic representation of flow zones (I, II, and III) of hydrodynamically escaping flow at $Kn_0 \ll 1$. The two zones of non-equilibrium flow, the Knudsen layer I and far field III, are divided by a quasi-isentropic zone II, where the flow can be approximately described by the IM given by Equations (5a), (10), and (11). With increasing Kn_0, the region of the quasi-isentropic flow gradually disappears. With increasing λ_0, the thickness of the Knudsen layer, δ_K, decreases, while the thickness of the subsonic flow region, δ_*, increases, so eventually δ_* becomes larger than δ_K. The boundaries between flow zones can be defined only approximately.

(A color version of this figure is available in the online journal.)

Parker's critical solution. Only when λ_0 approaches the largest Jeans parameter for which the flow remains hydrodynamic do the DSMC solutions tend to closely follow the critical solutions with $Ma > 1$ and $dMa/dr > 0$.

An interesting feature of the DSMC solution in a diatomic gas is that the flow becomes consistent with the subsonic part of Parker's (1963) critical solution as λ_0 approaches λ_c given by Equation (3): e.g., see the thick curve for $\lambda_0 = 2.7$ in Figure 7(b). Thus, the flow of a diatomic gas at small Kn_0 can include a subsonic region, where the solution closely follows the IM. Our DSMC simulations allow one to estimate the range of λ_0 as 2.1–2.9 for which this is applicable. In this range the DMSC solutions for a diatomic gas go through the critical point of Equation (17), where $Ma = 1$ and $\lambda = 2\gamma$. The degree of deviation of the DSMC solutions at Kn_0 larger than 10^{-3} is demonstrated in Figure 8. It confirms that $Kn_0 = 10^{-3}$ is the approximate upper limit for which there is a zone of nearly isentropic flow. The results in Figure 8 also show that the DSMC solutions do not approach the critical solution with decreasing Kn_0 if λ_0 is constant and sufficiently small with respect to λ_{c1}. However, the local Jeans parameter at the sonic surface weakly depends on Kn_0 if $Kn_0 \ll 10^{-2}$ and closely approaches λ_C when λ_0 increases and approaches the upper limit of the Jeans parameter for the hydrodynamic escape regime.

The presence of non-equilibrium zones, the Knudsen layer and far field, enables formation of an isentropic flow zone at small Kn_0 and arbitrary γ and λ_0 even if conditions given by Equation (19) are not satisfied. These conditions are obtained by analyzing the asymptotic behavior of the IM at $r \to 0$ and

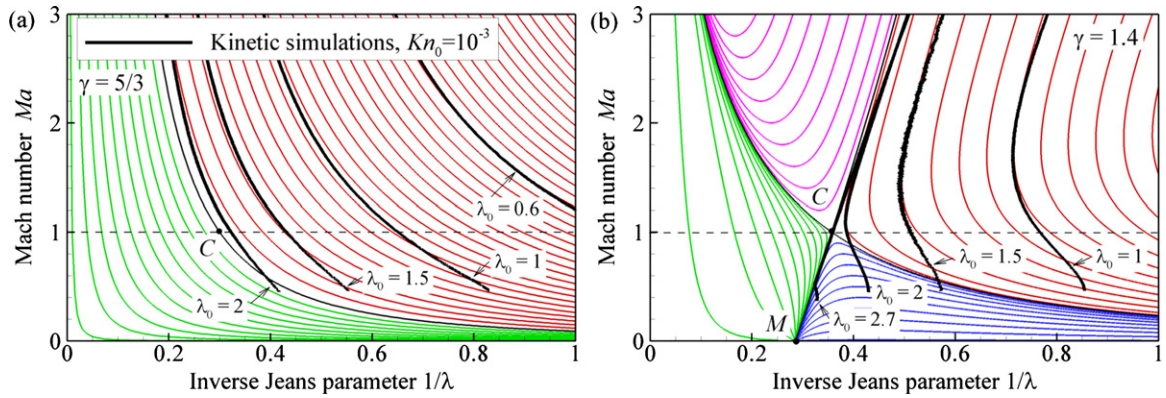

Figure 7. Flow structures in terms of the dependences $Ma = Ma(1/\lambda)$ (thick solid curves) found in kinetic simulations at $Kn_0 = 10^{-3}$ and various λ_0 for monatomic (a) and diatomic gases (b) shown together with the phase portraits of the IM (thin solid curves) taken from Figures 1(f) and (a). Kinetic simulations are performed with PM (a) and PMLB2 (b) models. The dashed line corresponds to $Ma = 1$.

(A color version of this figure is available in the online journal.)

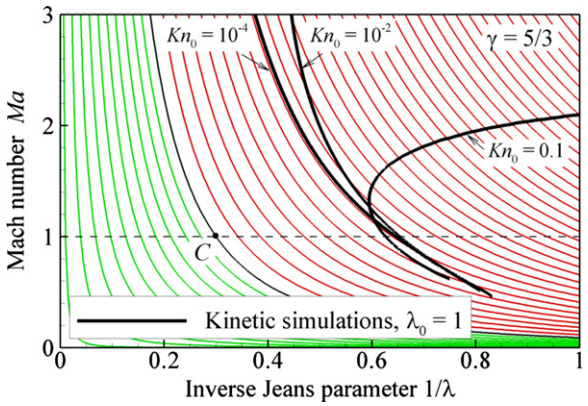

Figure 8. Flow structures in terms of the dependences $Ma = Ma(1/\lambda)$ (thick solid curves) found in kinetic simulations at $\lambda_0 = 1$ and various Kn_0 for a monatomic gas (PM model) shown together with the phase portraits of the IM (thin solid curves) taken from Figure 1(f). The dashed line corresponds to $Ma = 1$.

(A color version of this figure is available in the online journal.)

$r \to \infty$. This asymptotic behavior, however, is never realized, since the flow properties in the Knudsen layer and far field are qualitatively different from predicted by the IM. Namely, the gas flow attains supersonic or large subsonic velocities inside the Knudsen layer, so that the existence of a subsonic branch of the IM is not necessary. In particular, since at small Kn_0 the isentropic flow zone exists at $\lambda_0 \leqslant 2\gamma$, Parker's conditions cannot be used in order to obtain a lower limit for the possible range of masses or radii of planetary bodies as attempted for KBOs (Levi & Podolak 2009). In the far field, u, $T \to \text{const} > 0$ and, consequently, $\lambda \to 0$ at $r \to \infty$, irrespectively of the flow behavior at finite r. The latter, in particular, makes possible the existence of the supersonic isentropic flow zone at $\gamma > 3/2$, when u and $1/\lambda$ decrease with increasing r.

3.3. Comparison of Results of Kinetic Simulations with the Full and Reduced Navier–Stokes Models

The results of the DSMC simulations were also compared with the solutions of the time-dependent Navier–Stokes equations (4) found in the limit $t \to \infty$ (referred to as solutions of the full Navier–Stokes model) and the steady-state equations (5) with zero viscosity (referred to as solutions of the reduced Navier–Stokes model). The equations of the full Navier–Stokes model are solved with the splitting numerical methods, where advective terms are approximated with the Richtmayer or FLIC TVD (Flux Limiter Centered Total Variation Diminishing) schemes, and the diffusive terms are approximated by the central differences of the second order (Toro 1999) on a computational mesh with constant cell size $\Delta r/R_0 = 10^{-3} - 10^{-2}$. Three different lower boundaries are adopted for calculations: The source surface ($r = R_0$), sonic surface ($r = r_*$), and top of the Knudsen layer ($r = r_k$) given by Equation (20), which we will discuss in Section 3.4. The positions of the sonic surface and the top boundary of the Knudsen layer, as well as boundary values of n, u, and T at the lower boundary are set equal to the values found in the corresponding DSMC simulations. The equations for reduced Navier–Stokes model are solved numerically with the Runge-Kutta method of the second order with the spatial resolution $\Delta r/R_0 = 10^{-5} - 10^{-6}$. The initial conditions in this case are set at the top boundary of the Knudsen layer. The values of n and T at the lower boundary and the escape rates Φ_n and Φ_e were taken from results of corresponding DSMC simulations.

The calculations with the full and reduced Navier–Stokes models were performed at $Kn_0 = 10^{-4} - 10^{-1}$ in the full range of λ_0 under consideration for both mon- and diatomic gases. For a diatomic gas, it was assumed that the viscosity and thermal conductivity can be still calculated with equations for a monatomic gas, and, in particular, the Prandtl number $Pr = c_p\mu/\kappa$ is equal to 2/3. Although the latter is not completely accurate for a diatomic gas, our calculations reveal the same order of discrepancy between the full Navier–Stokes model and DSMC simulations for both gases. The results of these calculations are described below based on the typical example shown in Figure 9 for a monatomic gas of PM molecules.

It was found that the reduced steady-state Navier–Stokes model (thin dashed curves in Figure 9) is unsuitable for calculations of the flow structure in the blow-off regime. At fixed n and T at the lower boundary and fixed Φ_n and Φ_e taken from a DSMC simulation, the gas temperature in the solution of the reduced Navier–Stokes model goes to zero or infinity at finite, and fairly short, distance from the source, where the mean free path of gas molecules is still fairly small ($l/R_0 \approx 3.7 \cdot 10^{-3}$

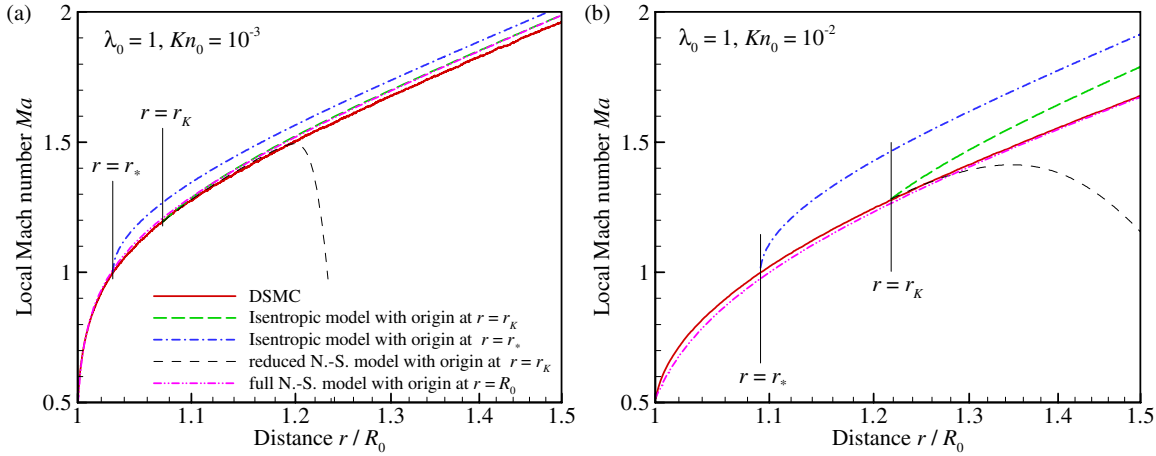

Figure 9. Comparison of distributions of the local Mach number Ma obtained in the DSMC simulations (solid curves, red) and applying the IM with origin at $r = r_K$ (dashed curves, green) and at $r = r_*$ (dash-dotted curves, blue), steady-state reduced Navier–Stokes (N.-S.) model with origin at $r = r_K$ (thin dashed curves, black), and time-dependent full Navier–Stokes model with origin at $r = R_0$ (dash-double-dotted curve, magenta) for the PM model at $\lambda_0 = 1$ and $Kn_0 = 10^{-3}$ (a) and $Kn_0 = 10^{-2}$ (b). The distributions of Ma obtained with the full Navier–Stokes model with origins at $r = r_*$ and $r = r_K$ are not plotted, but visually coincide with corresponding distributions obtained in the DSMC simulations. Solutions of the hydrodynamic models are obtained with initial or boundary conditions taken from the DSMC simulations. Vertical lines mark positions of the sonic surface, $r = r_*$, and the top of the Knudsen layer, $r = r_K$.

(A color version of this figure is available in the online journal.)

at $r/R_0 = 1.2$ in Figure 9(a)). Using the adjustment of Φ_e from the DSMC simulation cannot help to resolve this issue since the solution is very sensitive to Φ_e. In particular, the solution of the reduced Navier–Stokes model shown in Figure 9(a) was obtained by the trial-and-error adjustment of Φ_e with increments $10^{-6}\%$ (which is orders of magnitude smaller than the estimated level of numerical errors in Φ_e in our DSMC simulations). In spite of such a small increments, it was impossible to extend the solution of the reduced Navier–Stokes model with $T > 0$ in Figure 9(a) beyond $r/R_0 = \sim 1.25$.

On the other hand, a solution of the full Navier–Stokes model based on time-dependent equations with finite temperature at arbitrary large distance from the source can be obtained even if the lower boundary is taken directly at the source surface (dash-double-dotted curves in Figure 9). In our calculations, we were able to extend such solutions up to $r/R_0 = 40$ using sufficiently small time steps. At $Kn_0 = 10^{-3}$ this solution visually coincides with the DSMC solution inside the Knudsen layer, but in the isentropic flow zone the full Navier–Stokes model is visually indistinguishable from the solution obtained with the IM with origin at $r = r_K$. The solutions of the full Navier–Stokes model with origin at the sonic surface or at the top of the Knudsen layer (not shown in Figure 9) have orders-of-magnitude smaller discrepancy and visually coincides with the DSMC distributions up to the upper boundary of our DMSC computational domain. The advantage of the full Navier–Stokes model becomes apparent from the results for $Kn_0 = 10^{-2}$. Surprisingly, it still provides good approximation to results of kinetic simulations unlike the IM (Figure 9(b)). On the other hand, for $Kn_0 \geqslant 0.1$ the full Navier–Stokes model fails to predict the structure of rarefied flows. Similar results were obtained for different values of λ_0 and for a diatomic gas. Thus, the calculations showed the full Navier–Stokes model has no advantage over the simpler IM calculations at $Kn_0 = < 10^{-3} - 3 \cdot 10^{-3}$. It is superior to the IM only in the narrow range $Kn_0 = \sim 3 \cdot 10^{-3} - \sim 3 \cdot 10^{-2}$, in which the IM fails. At $Kn_0 > \sim 3 \cdot 10^{-2}$, flows do not contain a distinct Knudsen layer or a near equilibrium flow zone, as discussed earlier, so that kinetic simulations are required.

3.4. Structure of the Knudsen Layer

We have shown that the IM and full Navier–Stokes model alone are not capable of *predicting* blow-off. The good agreement between these models and the DSMC simulations reported in Sections 3.2 and 3.3 for $Kn_0 \leqslant 10^{-3}$ was achieved because the boundary (or initial) conditions were taken from the DSMC simulations. In spite of the fact the thickness of the Knudsen layer, δ_K, is of the order of a few tens of mean free paths (Figure 3) and, hence $\delta_K/R_0 \to 0$ at $Kn_0 \to 0$, this region cannot be ignored. Thus, any approximation of the flow field with the IM requires a determination of the flow parameters at the top of the Knudsen layer.

The structure of the Knudsen layer (Figure 10) at $0 < \lambda_0 < \sim 2$ resembles the structure of the Knudsen layer on a spherical body evaporating into vacuum at the absence of gravity (see, e.g., Cercignani 2000; Sone & Sugimoto 1993; Davidsson 2008; Lukianov & Khanlarov 2000). The distributions of n/n_0 and u/C_0 in both monatomic and diatomic gases are fairly close to each other in this region with the most important difference being a slower drop in $T_\perp/T_0$ and $T_{||}/T_0$ in the case of diatomic gas. This is a result of additional energy transfer from internal to translation degrees of freedom in a diatomic gas.

The thickness of the Knudsen layer, δ_K, is often thought to be on the order of the mean free path of gas molecules, since typically the local translational equilibrium is established after a local mean collision time. The results of the kinetic simulations without gravity, e.g., Lukianov & Khanlarov (2000) and our DSMC simulation at $\lambda_0 > 0$ (Figure 3) showed that the actual thickness of the Knudsen layer is at least an order of magnitude larger than l_0 as described earlier. Following Cattolica et al. (1974) and Lukianov & Khanlarov (2000), we calculate the position of the top boundary of the Knudsen layer $r_K = R_0 + \delta_K$ based on the criterion

$$\frac{3(T_{||}(r_K) - T_\perp(r_K))}{T_{||}(r_K) + 2T_\perp(r_K)} = -0.01. \qquad (20)$$

With decreasing Kn_0 for constant λ_0 gas parameters at the source surface, top boundary of the Knudsen layer, and sonic

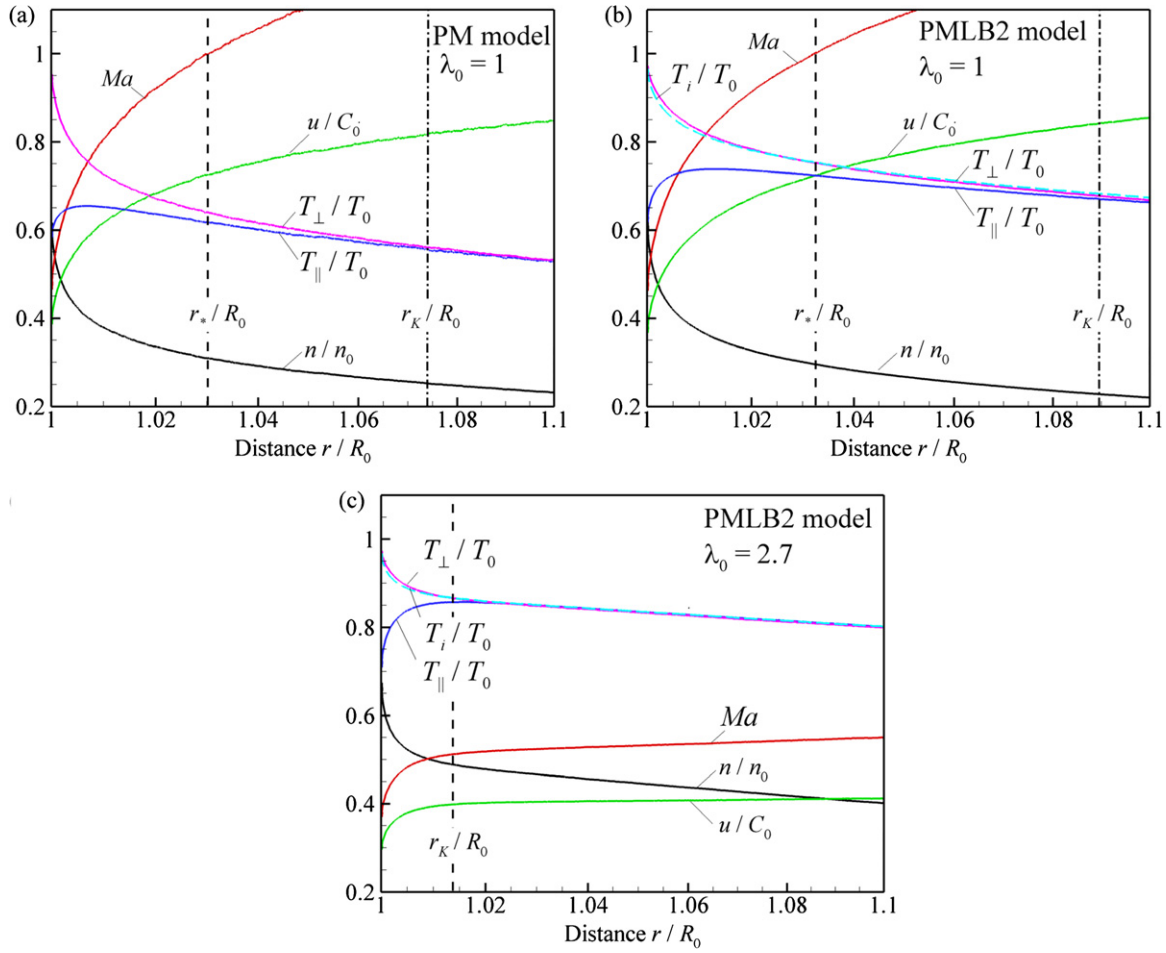

Figure 10. Distributions of density n/n_0, velocity u/C_0, local Mach number $Ma = u/\sqrt{\gamma kT/m}$, parallel, $T_\parallel/T_0$, and perpendicular, $T_\perp/T_0$, temperatures vs. distance r/R_0 inside the Knudsen layer found in kinetic simulations for monatomic (PM model, panel (a)) and diatomic (PMLB2 model, panels (b) and (c)) gases at $Kn_0 = 10^{-3}$ and $\lambda_0 = 1$ (panels (a) and (b)) and $\lambda_0 = 2.7$ (c). In panels (b) and (c), dashed curves show distribution of the temperature T_i/T_0 of internal degrees of freedom of diatomic molecules. Vertical lines mark positions of the sonic surface and the top of the Knudsen layer. $C_0 = \sqrt{2kT_0/m}$

(A color version of this figure is available in the online journal.)

surface tend to stabilize (Figure 11). In particular, the parameters at the source and sonic surface vary monotonically with Kn_0 but become nearly independent of Kn_0 at $Kn_0 < 10^{-3}$. The parameters at the top of the Knudsen layer vary non-monotonically and continue to change even around $Kn_0 = 10^{-5}$, the smallest Knudsen number considered in simulations. The thicknesses of Knudsen and subsonic layers, $\delta_K = r_K - R_0$ and $\delta_* = r_* - R_0$, for $Kn_0 < 10^{-3}$ are both two orders of magnitude larger than l_0. At moderate and large Kn_0 ($Kn_0 > \sim 10^{-4}$ in Figure 11(b)), the Mach number on the top of the Knudsen layer is supersonic, but at $Kn_0 < 10^{-3}$, δ_K weakly decreases, while δ_* increases approximately as $1/\sqrt{Kn_0}$ so that eventually the flow at the top of the Knudsen layer becomes subsonic with decreasing Kn_0. The transition from supersonic to subsonic flow at the top boundary of the Knudsen layer with decreasing Kn_0 is found for all λ_0 considered including the case of $\lambda_0 = 0$. The Mach number at the top of the Knudsen layer, Ma_K, is an important parameter for the application of hydrodynamic models. In particular, Anisimov (1968; see also Cercignani 1980, 2000) has shown that solving the flow in the Knudsen layer by the method of moments allows one to obtain all parameters at the top of the Knudsen layer as functions of the surface parameters and Ma_K. The dependences of parameters at the source surface, top of the Knudsen layer, and the sonic surface in a diatomic gas are qualitatively similar to dependences for a monatomic gas and are given in the Appendix.

The most important changes in the structure of the Knudsen layer occur when λ_0 approaches the upper limit of the blow-off regime. An increase in λ_0 (Figure 12) results in a substantial decrease in the thickness of the Knudsen layer and Ma_K, while n_K/n_0 and T_K/T_0 increase. Parameters at the sonic surface exhibit a weak variability with λ_0 for $\lambda_0 < 1.5$, while δ_* increases rapidly when λ_0 approaches the upper limit of the blow-off regime. As λ_0 increases with $Kn_0 = \text{const}$ the Mach number at the top of the Knudsen layer drops going from super- to subsonic flow at the top of the Knudsen layer. The value of λ_0 at which the flow at the top of the Knudsen layer becomes subsonic drops as Kn_0 decreases. Dependences of parameters at the top of the Knudsen layer and at the sonic surface on λ_0 in mon- and diatomic gases are close to each other quantitatively with exception of the thickness of the subsonic zone. In all simulations performed for a monatomic gas, δ_K and δ_* are the same order of magnitude and, in particular, the thickness of subsonic zone remains small as compared with R_0. For a diatomic gas, the flow can include an extended subsonic zone (Figure 10(c)), but only at $\lambda_0 > \sim 2.5$ (Figure 12(d)) where the actual Jeans parameter at the source surface, $\lambda(R_0) = \lambda_0 T_0/T(R_0)$, satisfy Equation (19b), i.e., $\lambda(R_0) > 2\gamma = 2.8$. Qualitatively, the

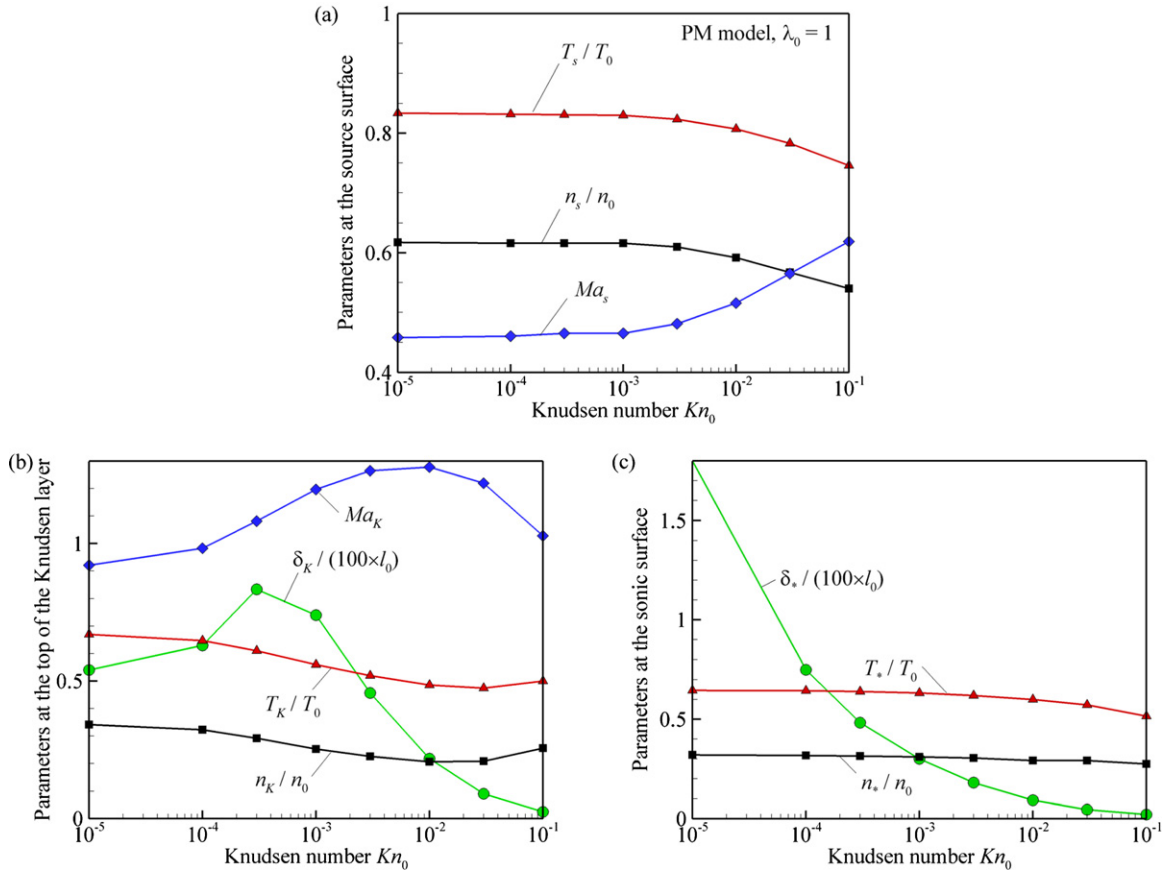

Figure 11. Parameters at the source surface ($r = R_0$, a), at the top of the Knudsen layer ($r = r_K = R_0 + \delta_K$, b), and at the sonic surface ($r = r_* = R_0 + \delta_*$, c) vs. Knudsen number Kn_0 found for a monatomic gas with the PM model at $\lambda_0 = 1$. Nominal thickness of the Knudsen layer, δ_K, is defined by the condition given by Equation (20). Curves with square (black), triangle (red), diamond (blue), and circle (green) symbols correspond to n_α/n_0, T_α/T_0, Ma_α, and δ_α/R_0, where subscript "α" denotes parameters at the surface ($\alpha = s$), top of the Knudsen layer ($\alpha = K$), and sonic surface ($\alpha = *$). In the text, gas parameters at the source surface are also denoted as $n(R_0)$, $T(R_0)$, and $Ma(R_0)$.

(A color version of this figure is available in the online journal.)

results shown in Figure 12(c) for a diatomic gas are in agreement with parameters at the top of the Knudsen layer found by Levi & Podolak (2009). They combined Parker's critical solution with the semi-analytical solution for the change of gas parameters across the Knudsen layer obtained by the method of moments (Cercignani 1980) for the range of λ_0 satisfying Equation (19b), i.e., for $2.8 < \lambda_0 < 3.5$ in a diatomic gas. Quantitatively, however, the results of the DSMC simulations are different from this solution. For instance, at $\lambda_0 = 2.8$, the DSMC simulations predict $Ma_K = 0.44$, while Levi & Podolak (2009) obtained $Ma_K = 1$.

3.5. Number and Energy Escape Rates

The calculation of escape rates is central to understanding atmospheric evolution. In Figures 13(a) and (b), the escape rates of a monatomic gas are represented in reduced unit using the number, $\Phi_{n0,0} = 4\pi R_0^2 n_0 \sqrt{kT_0/(2\pi m)}$, and energy, $\Phi_{e0,0} = 2kT_0\Phi_{n0,0}$, fluxes of molecules leaving the source surface as scaling parameters. These fluxes represent Jeans escape rates at the source surface at zero gravity.

When $Kn_0 \to \infty$, the flow gradually approaches the free-molecular state and the number escape rate Φ_n approached its value $\Phi_{n,0} = \Phi_{n0,0}(1+\lambda_0)\exp(-\lambda_0)$ specific for free-molecular flow, so that reduced values $\Phi_n/\Phi_{n0,0}$ diverge depending on λ_0. Quite remarkably, in the limit $Kn_0 \to 0$, the values of $\Phi_n/\Phi_{n0,0}$ tend to be independent of λ_0 and converge to the value for spherical expansion at zero gravity. The energy escape rate, $\Phi_e/\Phi_{e0,0}$, does not converge to a λ_0-independent value with decreasing Kn_0. On the other hand, we found that the energy loss rate, Φ'_e

$$\Phi'_e = \Phi_e + \frac{GMm}{R_0}\Phi_n, \tag{21}$$

where the contribution of the gravitational energy is removed (compare with Equation (5b)), becomes independent of the Jeans parameter at $Kn_0 \to 0$ (Figure 13(b)) and, obviously, also converges to a value which is specific for the spherical expansion at zero gravity. Thus, in the limit of small Kn_0, the linear dependence of the energy escape rate on λ_0 is given by the equation

$$\frac{\Phi_e}{\Phi_{e0,0}} = \frac{\Phi'_e}{\Phi_{e0,0}} - \frac{\lambda_0}{2}\frac{\Phi_n}{\Phi_{n0,0}}, \tag{22}$$

while $\Phi_n/\Phi_{n0,0}$ and $\Phi'_e/\Phi_{e0,0}$ approach constants that are determined by the intermolecular collision model. The dependences of the escape rates on λ_0 and Kn_0 in a diatomic gas are qualitatively similar to the dependences shown in Figure 13 and are given in the Appendix.

It is seen from Figures 13(a) and (b) that both $\Phi_n/\Phi_{n0,0}$ and $\Phi'_e/\Phi_{e0,0}$ still weakly vary with Kn_0 even at $Kn_0 \sim 10^{-4}$, so that simulations at finite Knudsen number cannot be used to determine the limiting values of $\Phi_n/\Phi_{n0,0}$ and $\Phi'_e/\Phi_{e0,0}$ at $Kn_0 \to 0$ (Table 1) with errors less than 1%–3%. As shown in

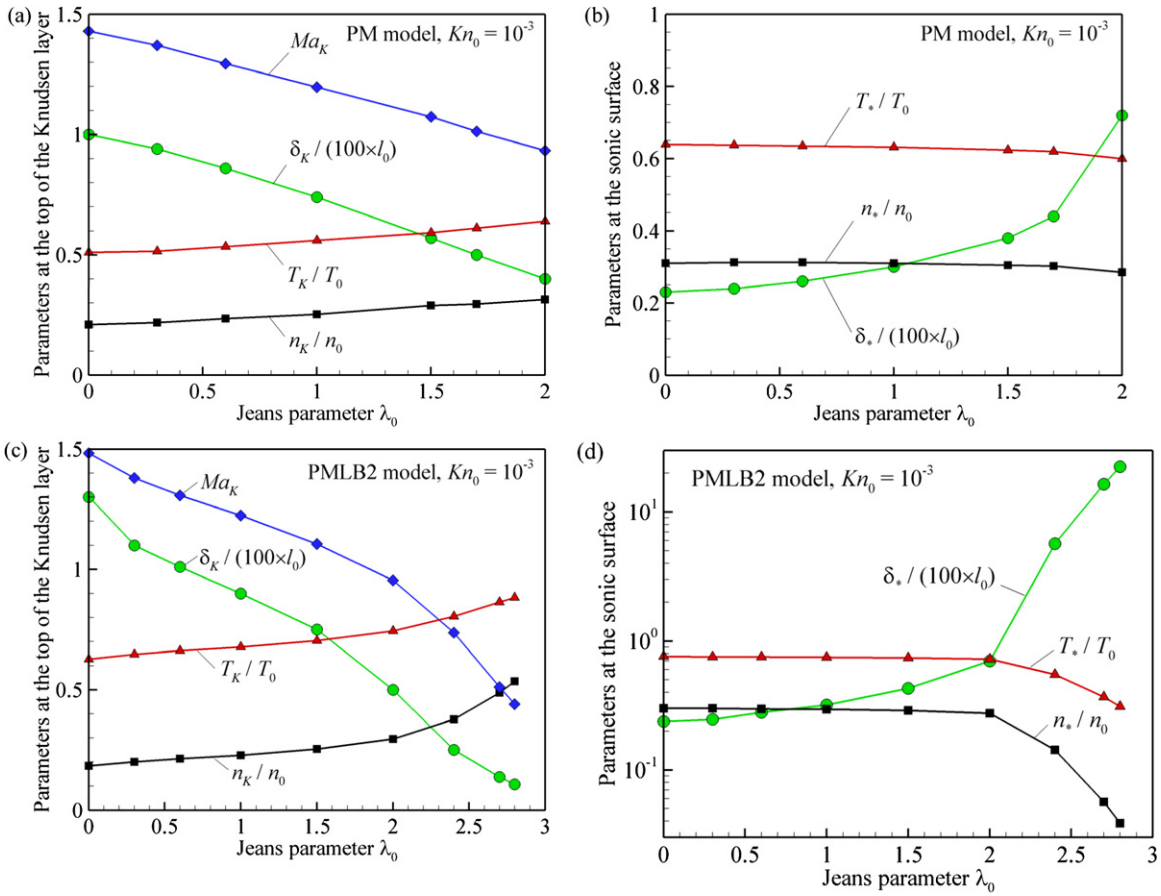

Figure 12. Parameters at the top of the Knudsen layer ($r = r_K = R_0 + \delta_K$, panels (a) and (c)) and at the sonic surface ($r = r_* = R_0 + \delta_*$, panels (b) and (d)) vs. Jeans parameter λ_0 found for a monatomic gas with the PM model (panels (a) and (b)) and for a diatomic gas with the PMLB2 model at $Kn_0 = 10^{-3}$ (panels (c) and (d)). Nominal thickness of the Knudsen layer, δ_K, is defined by the condition given by Equation (20). See notation of curves in the caption of Figure 11. Note the difference in the y-axis scale in panels (b) and (d).

(A color version of this figure is available in the online journal.)

Table 1
Values of Number Escape Rate, $\Phi_n/\Phi_{n0,0}$, and Energy Loss Rate, $\Phi'_e/\Phi_{e0,0}$ Obtained in the DSMC Simulations in the Limit $Kn_0 \to \infty$ with HS, PM, and PMLB2 Models

Model	$\Phi_n/\Phi_{n0,0}$	$\Phi'_e/\Phi_{e0,0}$	$\Phi'_e/(2kT_0\Phi_n)$	$\Phi'_e/((3+\zeta)kT_0\Phi_n)$	$\Phi'_e/((3+\zeta)kT_*\Phi_n)$
HS	0.838	0.899	1.07	0.713	1.11
PM	0.834	0.897	1.075	0.716	1.11
PMLB2	0.807	1.282	1.588	0.6352	0.84

Volkov et al. (2013), the calculated dependence of $\Phi_n/\Phi_{n0,0}$ on Kn_0 at $\lambda_0 = 0$ is in good quantitative agreement with results obtained by Bulgakova et al. (1997), so that the weak variation of $\Phi_n/\Phi_{n0,0}$ at small Knudsen numbers in our simulations presumably reflects the nature of the problem and is not caused by the simulation errors. It was found that the ratio Φ'_e/Φ_n, which represents the average sum of kinetic and internal energies of an escaping molecule, converges with decreasing Kn_0 faster than individual Φ'_e and Φ_n (Figure 13(c)). The difference in $\Phi'_e/(2kT_0\Phi_n)$ between mon- and diatomic gases is caused by the energy of internal degrees of freedom of molecules in the diatomic gas, so that values of $\Phi'_e/((3+\zeta)kT_0\Phi_n)$ for mon- and diatomic gases differ by only ~10% (Table 1).

The independence of $\Phi_n/\Phi_{n0,0}$ and $\Phi'_e/\Phi_{e0,0}$ on λ_0 at small Kn_0 is the characteristic feature of thermal escape in the hydrodynamic regime at $\lambda_0 < \lambda_{c1}$. As λ_0 increases above λ_{c1}, the number and energy escape rates rapidly drop (Volkov et al. 2011a). This drop indicates a transition to the Jeans-like escape regime. The DSMC simulations showed that at finite Kn_0 this transition takes place over a narrow range of λ_0. The independence of $\Phi_n/\Phi_{n0,0}$ and $\Phi'_e/\Phi_{e0,0}$ on λ_0, however, does not imply the flow parameters are independent of λ_0. On the contrary, the flow parameters continue to change with λ_0 (Figure 5).

4. EFFECTS OF ADDITIONAL OUTFLOW AND HEAT FLUX AT THE LOWER BOUNDARY

The boundary condition given by Equation (1) is well suited for atmospheric blow-off driven by the surface sublimation of an icy body such as comets, KBOs, satellites of close-in exoplanets (Cassidy et al. 2009), and, possibly, the early evolution of satellites of giant planets like Io. For such bodies the lower boundary of the computational domain coincides with real sublimating surface. The boundary conditions in Equation (1) are only approximate for a virtual boundary in an atmosphere at

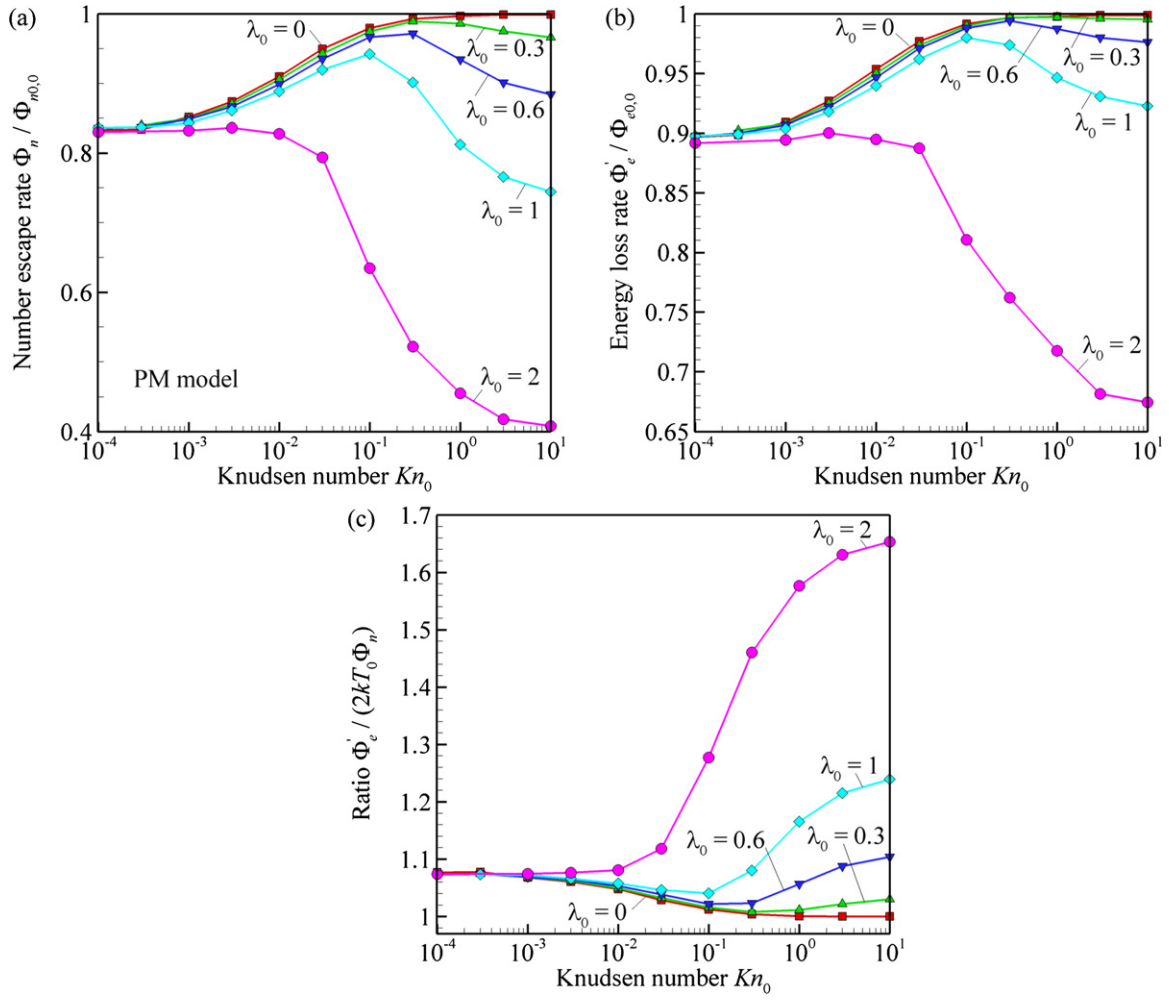

Figure 13. Number escape rate $\Phi_n/\Phi_{n0,0}$ (a), energy loss rate $\Phi_e'/\Phi_{e0,0}$ (b), and the ratio $\Phi_e'/(2kT_0\Phi_n)$ (c) vs. Knudsen number Kn_0 found in the DSMC simulations for a monatomic gas based on PM model at $\lambda_0 = 0$ (square symbols), $\lambda_0 = 0.3$ (triangle symbols), $\lambda_0 = 0.6$ (nabla symbols), $\lambda_0 = 1$ (diamond symbols), and $\lambda_0 = 2$ (circle symbols).

(A color version of this figure is available in the online journal.)

which the flow is small and above which little additional solar energy is absorbed. If the flow across this boundary is not small the simple evaporative-type boundary conditions in Equation (1) should be corrected. The parameters at the lower boundary of the blow-off flow domain, however, can be found only by considering the flow below that boundary. In this section, we pursue a less ambitious goal. Namely, we parametrically study the sensitivity of hydrodynamically escaping flows to adding a net flow and heat flux at the lower boundary of the computational domain. The effect of an added heat flow in the Jeans-like regime was explored for large λ_0 in Titan's atmosphere (Tucker & Johnson 2009).

Here we assume small deviations from equilibrium in the velocity distribution of gas molecules entering the computational domain through its lower boundary by replacing Equation (1) with the Chapman–Enskog distribution (Chapman & Cowling 1970). Since the viscous stresses in a one-dimensional atmosphere are usually negligible, we account only for the presence of a fixed radial velocity u_0 and heat flux q_0 only in the distribution function and then solve the resulting flow. Then the boundary condition at $r = R_0$ takes the form:

$$\text{at } v_{||} > 0: \quad f(R_0, v_{||}, v_\perp, \varepsilon_i, t) = \tilde{f}_{0t}(v_{||} - u_0, v_\perp)\tilde{f}_{0i}(\varepsilon_i), \tag{23a}$$

where

$$\tilde{f}_{0t}(c_{||}, c_\perp) = \frac{n_0}{(2\pi kT_0/m)^{3/2}} \exp\left(-\frac{m\left(c_{||}^2 + c_\perp^2\right)}{2kT_0}\right) \times \left[1 - \frac{q_0 m c_{||}}{n_0 (kT_0)^2}\left(1 - \frac{1}{5}\frac{m\left(c_{||}^2 + c_\perp^2\right)}{kT_0}\right)\right]. \tag{23b}$$

For a monatomic gas the distribution, $\tilde{f}_{0i}(\varepsilon_i)$ is replaced by 1. The boundary conditions given by Equation (23) introduce two additional dimensionless parameters that can be given in the form of the Mach number $Ma_0 = u_0/\sqrt{\gamma kT_0/m}$ and dimensionless heat flux $Q_0 = q_0/(n_0 kT_0\sqrt{kT_0/m})$. The velocity distribution given by Equation (23b) is valid only for small deviations from equilibrium when Q_0 does not exceed a value on the order of 0.1 (Garcia & Alder 1998). For larger Q_0, $\tilde{f}_{0t}(c_{||}, c_\perp)$ may take negative values at relatively small $c_{||}/\sqrt{kT_0/m}$, which has no physical meaning. Accounting for the restriction $Q_0 < 0.1$, the acceptance–rejection method developed by Garcia & Alder (1998) is used in the DSMC simulations in order to sample velocities of molecules entering the computational domain through the lower boundary with the

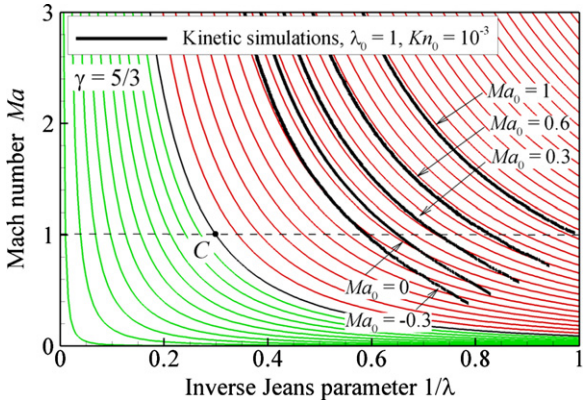

Figure 14. Flow structures in terms of the dependences $Ma = Ma(1/\lambda)$ (thick solid curves) found in kinetic simulations with the boundary condition given by Equation (23) with varying Ma_0 and $Q_0 = 0$ shown together with the phase portraits of the IM (thin solid curves) taken from Figure 1(f). Kinetic simulations are performed with the PM model at $\lambda_0 = 1$ and $Kn_0 = 10^{-3}$. The dashed line corresponds to $Ma = 1$.

(A color version of this figure is available in the online journal.)

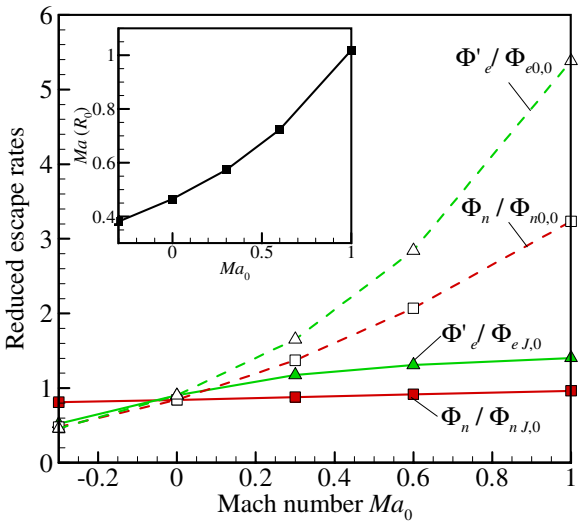

Figure 15. Scaled number escape rate Φ_n (square symbols) and energy loss rate Φ'_e (triangle symbols) vs. the Mach number Ma_0 found in the DSMC simulations with boundary condition given by Equation (23) and the PM model at $\lambda_0 = 1$, $Kn_0 = 10^{-3}$, and $Q_0 = 0$. Dashed curves with open symbols correspond to the calculated values scaled with the Jeans number and energy rates at the source at zero gravity, $\Phi_{n0,0}$ and $\Phi_{e0,0}$. Solid curves with bold symbols correspond to the same rates scaled with the modified Jeans escape rates at the source at zero gravity, $\Phi_{nJ,0}$ and $\Phi_{eJ,0}$, given by Equation (24). Inset shows $Ma(R_0)$ vs. Ma_0.

(A color version of this figure is available in the online journal.)

velocity distribution given by Equation (23b). It is worth noting that the actual values of gas parameters at the source surface such as $n(R_0)$, $T(R_0)$, $u(R_0)$, and $Ma(R_0) = u(R_0)/\sqrt{\gamma kT(R_0)/m}$ are not equal to parameters n_0, T_0, and u_0 of Equation (23) and Ma_0, since the distribution function of molecules returning to the surface does not coincide with the distribution function of outgoing molecules given by Equation (23).

Fixing Ma_0 and Q_0 in the distribution function for values of λ_0 in the blow-off regime, a series of kinetic simulations with the boundary conditions given by Equation (23) were performed for $-0.3 \leqslant Ma_0 \leqslant 1$ at $Q_0 = 0$ and for $0 \leqslant Q_0 \leqslant 0.1$ at $Ma_0 = 0$. As the gas attempts to overcome gravity, these led, not surprisingly, to increased values of $Ma(R_0)$ for the same Kn_0 and λ_0. It was found that the effect on the flow structure and the escape rates of fixing Q_0 in the distribution function is very small. This is in agreement with the fact that the heat flux contribution into the net energy balance given by Equation (5b) in the hydrodynamic regime is small. Fixing Ma_0, on the other hand, induces significant changes in both the flow field (Figure 14) and the escape rates (Figure 15). This is expected since adding a fixed Ma_0 into the distribution function for the same λ_0 and Kn_0 results in a strong increase of the initial enthalpy of fluid particles at the source surface. With Ma_0 increasing from 0 to 1, the Knudsen layer at the source surface gradually disappears and $Ma(R_0)$ approaches Ma_0 (inset in Figure 15). With increasing Ma_0 at fixed λ_0, however, the DSMC solution on the plane $(Ma, 1/\lambda)$ shifts further away from Parker's critical solution. The results of the DSMC simulations for a monatomic gas suggest that with variation of Ma_0 and λ_0 at small Kn_0 any point on the plane $(Ma, 1/\lambda)$ in the domain of the solution family I with $Ma > 1$ can be reached with the isentropic flow.

The reduced number escape rate $\Phi_n/\Phi_{n0,0}$ and energy loss rate $\Phi'_e/\Phi_{e0,0}$ exhibit a strong, close to quadratic, dependence on Ma_0. Although many factors contribute to the change of the rates with varying Ma_0 (or $Ma(R_0)$), the primary effect is found to be directly related to net change in the radial velocity of molecules leaving the source according to Equation (23). By analogy with $\Phi_{n0,0}$ and $\Phi_{e0,0}$ for the case $Ma_0 = 0$, one can introduce the modified Jeans number and energy escape rates (Yelle 2004; Volkov et al. 2011b), which are equal to the number and energy fluxes of molecules, leaving the surface with the boundary condition given by Equation (23) at $q_0 = 0$ and zero gravity:

$$\Phi_{nJ,0} = \Phi_{n0,0}\left[\exp\left(-S_0^2\right) + \sqrt{\pi}S_0(1 + \mathrm{erf}(S_0))\right], \quad (24a)$$

$$\Phi_{eJ,0} = \Phi_{e0,0}\left[\left(1 + 2S_0^2\right)\exp\left(-S_0^2\right) + \sqrt{\pi}S_0\left(1 + S_0^2/2\right)(1 + \mathrm{erf}(S_0))\right], \quad (24b)$$

where $S_0 = u_0/\sqrt{2kT_0/m} = \sqrt{\gamma/2}Ma_0$ and $\mathrm{erf}(S) = (2/\sqrt{\pi})\int_0^S \exp(-x^2)dx$ is the error function. Equation (24) can be obtained by inserting the velocity distribution given by Equation (23) with $q_0 = 0$ into the kinetic definitions of the escape rates (see Volkov et al. 2011b for details on the number escape rate; calculation of the energy escape rate can be performed by analogy) at the source surface and assuming $\lambda_0 = 0$. One can see then that the reduced rates in the form $\Phi_n/\Phi_{nJ,0}$ and $\Phi'_e/\Phi_{eJ,0}$ demonstrate only moderate variations with Ma_0 around their values characteristic for the case $Ma_0 = 0$ (solid curves with bold symbols in Figure 15). In particular, $\Phi_n/\Phi_{nJ,0}$ varies only from ~0.846 to ~0.964 when Ma_0 increases from 0 to 1.

5. CONCLUSION

Our kinetic simulations showed that at small Knudsen numbers at the source surface a near equilibrium zone of one-dimensional hydrodynamically escaping atmospheric flow for both mon- and diatomic gases is formed. This zone can be accurately described using the IM and appropriate boundary conditions for all Jeans parameters in hydrodynamic escape regime ($\lambda_0 <$ ~2.1 and $\lambda_0 <$ ~2.8 for mon- and diatomic gases, respectively; see Volkov et al. 2011a, 2011b, 2013). We also showed that an isentropic flow zone exists only if the Knudsen

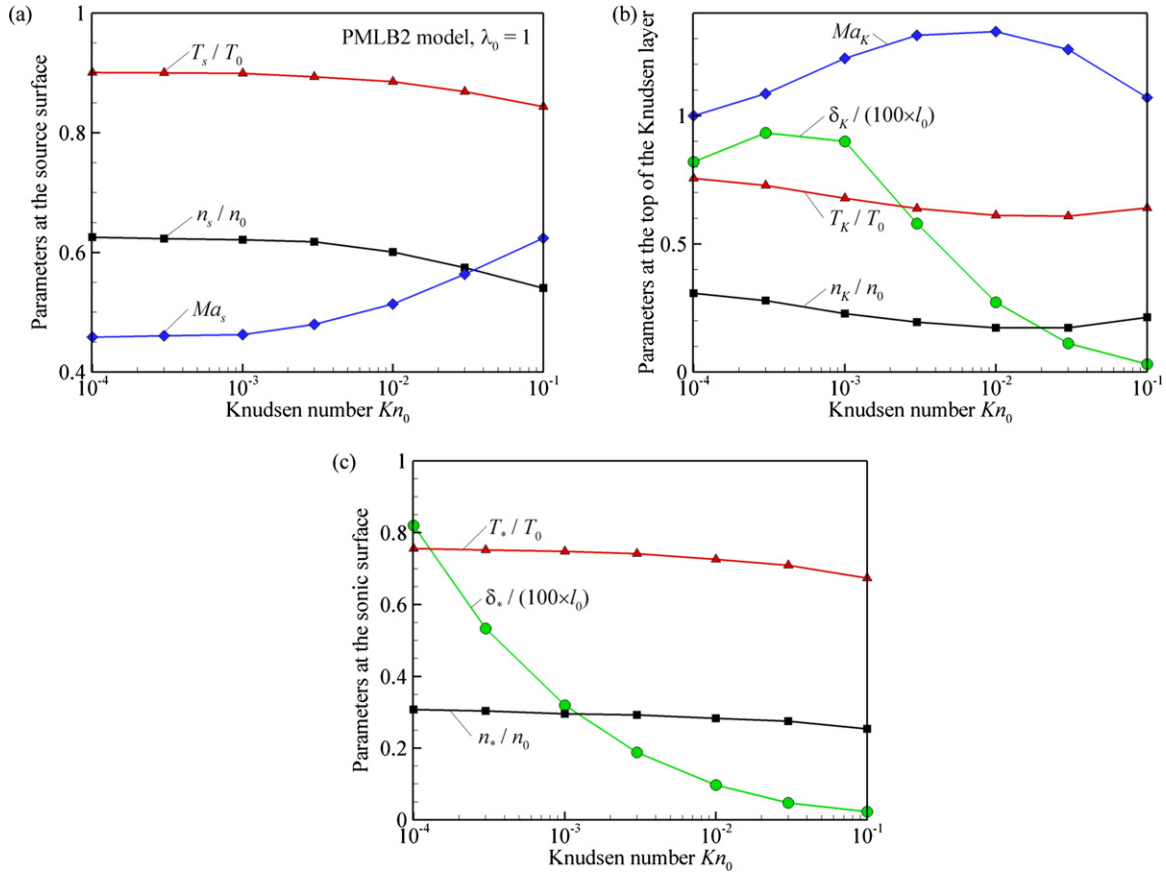

Figure 16. Parameters at the source surface ($r = R_0$, panel (a)), at the top of the Knudsen layer ($r = r_K = R_0 + \delta_K$, panel (b)), and at the sonic surface ($r = r_* = R_0 + \delta_*$, panel (c)) vs. Knudsen number Kn_0 found for a diatomic gas with the PMLB2 model at $\lambda_0 = 1$. Nominal thickness of the Knudsen layer, δ_K, is defined by the condition given by Equation (20). Curves with square (black online), triangle (red), diamond (blue), and circle (green) symbols correspond to n_α/n_0, T_α/T_0, Ma_α, and δ_α/R_0, where subscript "α" denotes parameters at the source surface ($\alpha = s$), top of the Knudsen layer ($\alpha = K$), and sonic surface ($\alpha = *$). In the text, gas parameters at the source surface are also denoted as $n(R_0)$, $T(R_0)$, and $Ma(R_0)$.

(A color version of this figure is available in the online journal.)

number at the source surface does not exceed $10^{-3} - 3 \cdot 10^{-3}$, and above this limit the IM cannot be used for predictions of the flow structure, unlike what was assumed in the modeling of highly rarefied KBO atmospheres (Levi & Podolak 2009). When the source Knudsen number is less than $10^{-3} - 3 \cdot 10^{-3}$, the isentropic flow zone is surrounded by two essentially non-equilibrium flow zones, the Knudsen layer at the source surface and a highly rarefied far field (Figure 6). However, this is often ignored and the isentropic flow model is used alone to predict the flow structure, although attempts to account for the rarefaction at large altitudes have been included (e.g., Chassefière 1996a, 1996b; Yelle 2004). Here, we show that the Knudsen layer cannot be ignored even in the limit of infinitely small Knudsen numbers. This is a result of the non-equilibrium nature of the flow in the Knudsen layer, where both enthalpy and entropy substantially change, so that the parameters at the bottom of the isentropic flow zone always differ from parameters at the source surface. These results are directly applicable to recent efforts (e.g., Stern & Trafton 2008; Levi & Podolak 2009, 2011) to model sublimation-driven atmospheres on KBO-like objects, for which the EUV heating is often insignificant. If there is significant heating in the simulation region that overwhelms the changes in the enthalpy, then a hydrodynamic model starting at the source surface can in principle give a reasonable description of the flow structure. This can be the case, for instance, for modeling of atmospheres of planets orbiting close to their parent star (Murray-Clay et al. 2009; Koskinen et al. 2012).

For the cases studied here in which there is no heating in the simulation region it is shown that all families of solutions of the IM for the spherical flows in the gravitational field can be classified and analyzed in terms of the local Mach number and Jeans parameter. Any solution of the IM in that form is unique for a given number of internal degrees of freedom and does not depend on other flow parameters. Using this we found that Parker's (1963) theory of isentropic flow in the gravitational field, which is based on the choice of the critical solution satisfying the condition of monotonically increasing velocity, fails to predict the results of kinetic simulations for both mon- and diatomic gases. With arbitrary source Jeans parameters, the kinetic solutions follow the IM, but do not coincide with Parker's (1963) critical solution. Only when the Jeans parameter at the source approaches the upper limit for the hydrodynamic regime of thermal escape, does the solution of the kinetic model approach Parker's critical solution. Moreover, in a monatomic gas, the flow velocity can decrease with distance, while the local Jeans parameter increases in accordance with the general solution of the IM. At the same time it is found that the local Mach number, but not the gas velocity, is an increasing function of distance in all kinetic simulations performed.

We have shown that the real asymptotic behavior in the outflow of a neutral gas does not typically follow the hydrodynamic models including the IM, a fact that was extensively argued in the past. In particular, the long discussion on the applicability of the evaporative and hydrodynamic escape (e.g., Chamberlain

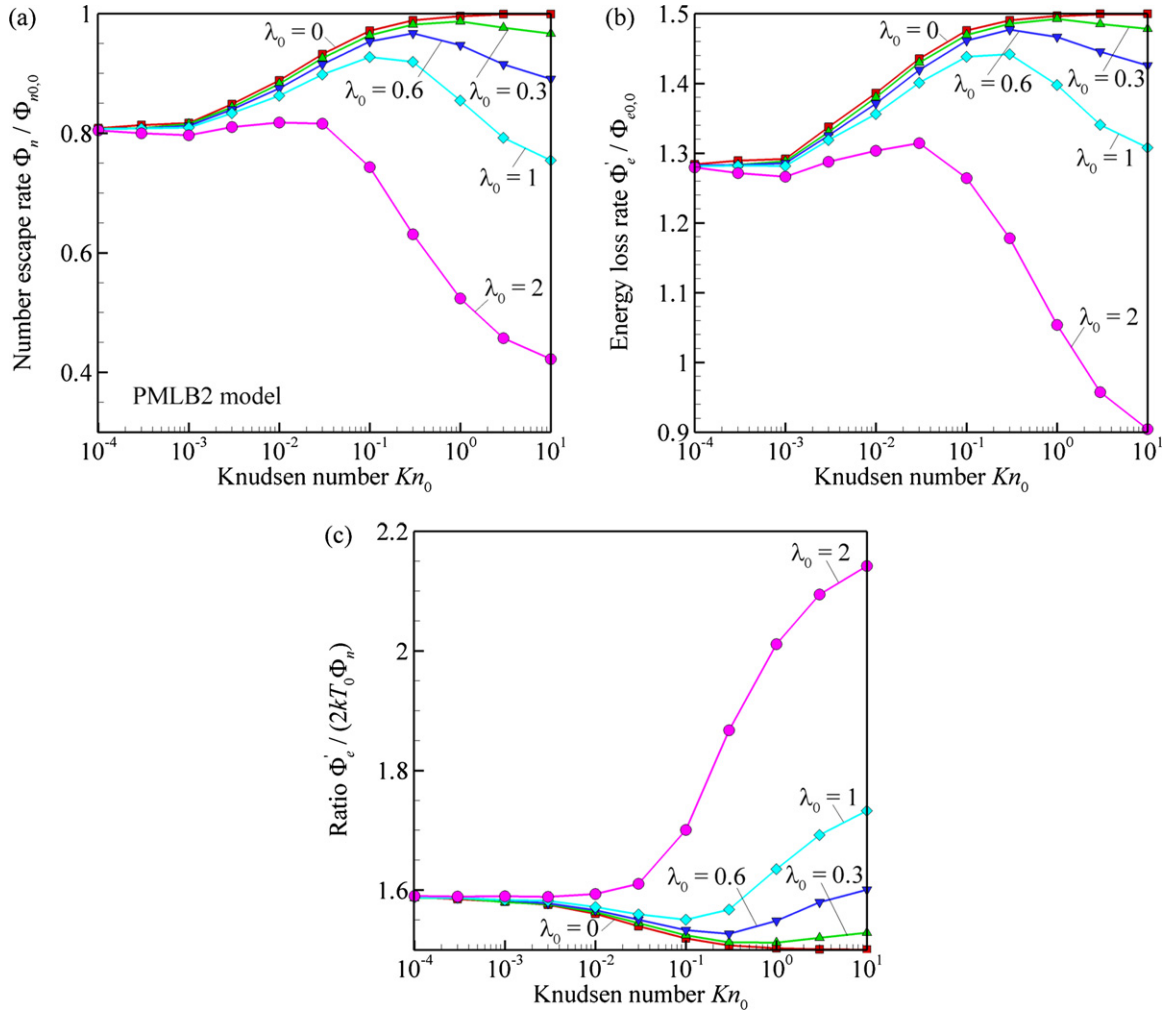

Figure 17. Number escape rate $\Phi_n/\Phi_{n0,0}$ (a), energy loss rate $\Phi'_e/\Phi_{e0,0}$ (b), and the ratio $\Phi'_e/(2kT_0\Phi_n)$ (c) vs. Knudsen number Kn_0 found in the DSMC simulations for a monatomic gas based on PMLB2 model at $\lambda_0 = 0$ (square symbols), $\lambda_0 = 0.3$ (triangle symbols), $\lambda_0 = 0.6$ (nabla symbols), $\lambda_0 = 1$ (diamond symbols), and $\lambda_0 = 2$ (circle symbols).

(A color version of this figure is available in the online journal.)

1965; Parker 1965; Carovillano & King 1965) was stimulated to a large extent by the analysis of the possible asymptotic behavior of the hydrodynamic model at large distances from the source. This behavior can make sense for coronal outflow of plasma or stellar winds in which the Coulomb cross section keeps the plasma collisional even if density approaches zero (Parker 1963; Murray-Clay et al. 2009). For atmospheric outflow of a neutral gas, where the mean free path of gas molecules increases roughly inversely proportional to the drop in the gas density with the distance from the source, hydrodynamic equilibrium models become inapplicable as $r \to \infty$. The presence of two non-equilibrium zones, the Knudsen layer and the far field, enables the existence of the isentropic flow between them even if Parker's conditions given by Equation (19) are not satisfied since these conditions are derived based on the analysis the asymptotic behavior of the IM at $r \to 0$ and $r \to \infty$, which is irrelevant to the blow-off of the neutral gas.

Kinetic simulations showed that the structure of the Knudsen layer depends on the strength of the gravitational field. With decreasing Knudsen number at the source, the thickness of the subsonic flow layer decreases faster than the thickness of the Knudsen layer. Simultaneously, with an increase in the strength of the gravitational field and, correspondingly, in the source Jeans parameter, the thickness of the subsonic layer increases while the thickness of the Knudsen layer decreases. As a result, the flows of both mon- and diatomic gases at the top of the Knudsen layer eventually become subsonic with decreasing Knudsen number or increasing Jeans parameter. In a monatomic gas the thicknesses of subsonic and Knudsen layers are the same order of magnitude. In a diatomic gas a relatively long subsonic zone may exist, where the flow closely follows Parker's critical solution, but only in a narrow range of the Jeans parameter, from ~2.5 to ~2.8, which is close to the transition to the Jean-like escape. The parameters at the top of the Knudsen layer, given here as functions of the source Knudsen number and Jeans parameter, can be used as boundary conditions for continuum models of hydrodynamics escape when the principal heat source is below the lower boundary of the simulations region as well as from sublimation-driven atmospheres of KBO. This approach enables accurate calculation of the atmospheric structure and escape rate avoiding computationally expensive kinetic simulations.

Although the general structure of a hydrodynamic outflow essentially depends on the Jeans parameters, the number and

energy loss rates at $\lambda_0 \leqslant \lambda_{c1}$ are nearly independent of the Jeans parameter in the limit of small Knudsen number, where their reduced values become constant. This property is characteristic of hydrodynamically escaping flows and not valid for Jeans-like escape. The constant reduced rates in the limit of small Knudsen numbers are completely defined by the model of intermolecular collisions and coincide with the number and energy loss rates in the flows at zero gravity.

Kinetic simulations performed with the Chapman–Enskog velocity distribution function used as a boundary condition at the lower boundary showed that the additional outflow velocity and heat flux imposed at the lower boundary do not result in qualitative changes in the flow field. Whereas the net effect of the additional heat flux is found to be small, an added upward flow speed induces a decrease in the thickness of the Knudsen layer and an increase in the number and energy loss rates. These loss rates, however, if scaled with the modified Jeans number and energy escape rates at the source surface at zero gravity given by Equation (24), are only slightly different from the rates found with the evaporative-type boundary condition.

In our kinetic simulations for a monatomic gas, the thickness of the subsonic flow zone remains small regardless of the inflow velocity at the lower boundary. This suggests that the extended subsonic zone of hydrodynamically escaping hydrogen predicted in hydrodynamic simulations of an atmosphere on a close-in exoplanet (e.g., Murray-Clay et al. 2009; Koskinen et al. 2012) can be attributed to the non-negligible effect of the net heating of the rarefied part of the atmosphere due to absorption of the stellar radiation. The kinetic modeling of atmospheric flows with external heating is a subject of our current work.

This research was supported by the NASA Planetary Atmospheres Program and the NSF Astronomy Program. Computational support is provided by the Oak Ridge Leadership Computing Facility (project MAT009) and the National Science Foundation through the Extreme Science and Engineering Discovery Environment (project TGDMR110090).

APPENDIX

PARAMETERS AT THE SOURCE SURFACE, TOP OF THE KNUDSEN LAYER, AND SONIC SURFACE AND ESCAPE RATES IN THE FLOWS OF A DIATOMIC GAS

Figure 16 demonstrates parameters at the source surface, top of the Knudsen layer, and sonic surface as functions of the Knudsen number in a diatomic gas. The number and energy escape rates in a diatomic gas in a range of the Knudsen number and Jeans parameter are shown in Figure 17. These results are complimentary to the dependences for a monatomic gas shown in Figures 11 and 13.

REFERENCES

Anisimov, S. I. 1968, Sov. Phys.—JETP, 27, 182
Bird, G. A. 1994, Molecular Gas Dynamics and the Direct Simulation of Gas Flows (Oxford: Clarendon)
Borgnakke, C., & Larsen, P. S. 1975, JCoPhJ, 18, 405
Bulgakova, N. M., Plotnikov, M. Yu., & Rebrov, A. K. 1997, FlDy, 32, 870
Carovillano, R. L., & King, J. H. 1965, ApJ, 141, 526
Cassidy, T. A., Mendez, R., Arras, P., Johnson, R. E., & Skrutskie, M. F. 2009, ApJ, 704, 1341
Cattolica, R., Robben, F., Talbot, L., & Willis, D. R. 1974, PhFl, 17, 1793
Cercignani, C. 1980, in Technical papers selected from the 12th Int. Symp. on Rarefied Gas Dynamics, ed. S. S. Fisher (New York: AIAA), Progress in Astronautics and Aeronautics 74, 305
Cercignani, C. 2000, Rarefied Gas Dynamics: From Basic Concepts to Actual Calculations (Cambridge: Cambridge Univ. Press)
Chamberlain, J. W. 1963, P&SS, 11, 901
Chamberlain, J. W. 1965, ApJ, 141, 320
Chapman, S., & Cowling, T. G. 1970, The Mathematical Theory of Non-Uniform Gases (3rd ed.; Cambridge: Cambridge Univ. Press)
Chassefière, E. 1996a, JGR, 101, 26039
Chassefière, E. 1996b, Icar, 124, 537
Combi, M. R., Tenishev, V. M., Rubin, M., Fougere, N., & Gombosi, T. I. 2012, ApJ, 749, 29
Crifo, J. F., Lukianov, G. A., Rodionov, A. V., Khanlarov, G. O., & Zakharov, V. V. 2002, Icar, 156, 249
Davidsson, B. J. R. 2008, SSRv, 138, 207
Edwards, R. H., & Cheng, H. K. 1966, AIAAJ, 4, 558
Ferziger, J. H., & Kaper, H. G. 1972, Mathematical Theory of Transport Processes in Gases (Amsterdam: North-Holland)
Fletcher, C. A. J. 1991, Computational Techniques for Fluid Dynamics, Vol. 2 (2nd ed.; Amsterdam: Springer)
Garcia, A. L., & Alder, B. J. 1998, JCoPh, 140, 66
Hamel, B. B., & Willis, D. R. 1966, PhFl, 9, 829
Hinshelwood, C. N. 1940, The Kinetics of Chemical Change (Oxford: Clarendon)
Hunten, D. M. 1982, P&SS, 30, 773
Hunten, D. M., Pepin, R. O., & Walker, J. C. G. 1987, Icar, 69, 532
Johnson, R. E., Combi, M. R., Fox, J. L., et al. 2008, SSRv, 139, 355
Koskinen, T. T., Harris, M. J., Yelle, R. V., & Lavvas, P. 2012, doi: 10.1016/j.icarus.2012.09.026
Krasnopolsky, V. A. 1999, JGR, 104, 5955
Lammer, H., Kasting, J. F., Chassefière, E., et al. 2008, SSRv, 139, 399
Lammer, H., Odert, P., Leitzinger, M., et al. 2009, A&A, 506, 399
Lemaire, J. 1966, AnAP, 29, 197
Levi, A., & Podolak, M. 2009, Icar, 202, 681
Levi, A., & Podolak, M. 2011, Icar, 214, 308
Linsky, J. L., Yang, H., France, K., et al. 2010, ApJ, 717, 1291
Lukianov, G. A., & Khanlarov, Gr. O. 2000, ThAe, 7, 489
Marov, M. Ya., Shematovich, V. I., & Bisicalo, D. V. 1996, SSRv, 76, 1
Muñoz, A. G. 2007, P&SS, 55, 1426
Murray-Clay, R. A., Chiang, E. I., & Murray, N. 2009, ApJ, 693, 23
Öpik, E. J. 1963, GeoJRAS, 7, 490
Öpik, E. J., & Singer, S. F. 1961, PhFl, 4, 221
Parker, E. N. 1960, ApJ, 132, 821
Parker, E. N. 1963, Interplanetary Dynamical Processes (New York: Interscience)
Parker, E. N. 1964a, ApJ, 139, 72
Parker, E. N. 1964b, ApJ, 139, 93
Parker, E. N. 1965, ApJ, 141, 322
Penz, T., Erkaev, N. V., Kulikov, Yu. N., et al. 2008, P&SS, 56, 1260
Schläppi, B., Altwegg, K., & Wurz, P. 2008, Icar, 195, 674
Sedov, L. I. 1997, Mechanics of Continuous Media, Vol. 1 (Singapore: World Scientific)
Sone, Y., & Sugimoto, H. 1993, PhFlA, 5, 1491
Stern, S. A., & Trafton, L. M. 2008, in The Solar System Beyond Neptune, ed. M. A. Barucci, H. Boehnhardt, D. P. Cruikshank, & A. Morbidelli (Tucson, AZ: Univ. Arizona), 365
Stone, J. M., & Proga, D. 2009, ApJ, 694, 205
Tenishev, V., Combi, M., & Davidsson, B. 2008, ApJ, 685, 659
Tian, F. 2009, ApJ, 703, 905
Tian, F., Toon, O. B., Pavlov, A. A., & De Sterck, H. 2005, ApJ, 621, 1049
Toro, E. F. 1999, Solvers and Numerical Methods for Fluid Dynamics: A Practical Introduction (2nd ed.; Berlin: Springer)
Tucker, O. J., Erwin, J. T., Deighan, J. I., Volkov, A. N., & Johnson, R. E. 2012, Icar, 217, 408
Tucker, O. J., & Johnson, R. E. 2009, P&SS, 57, 1889
Vidal-Madjar, A., Désert, J.-M., Lecavelier des Etangs, A., et al. 2004, ApJL, 604, L69
Vidal-Madjar, A., Lecavelier des Etangs, A., Désert, J.-M., et al. 2003, Natur, 422, 143
Volkov, A. N., & Lukyanov, G. A. 2007, in 25th Int. Symp. Rarefied Gas Dynamics, ed. M. Ivanov & A. Rebrov (Saint Petersburg, Novosibirsk, Russia: Publishing House of the Siberian Branch of the Russian Academy of Sciences), 1203
Volkov, A. N., Johnson, R. E., Tucker, O. J., & Erwin, J. T. 2011a, ApJL, 729, L24
Volkov, A. N., Sevilla, C., & Zhigilei, L. V. 2007, ApSS, 253, 6394
Volkov, A. N., Tucker, O. J., Erwin, J. T., & Johnson, R. E. 2011b, PhFl, 23, 066601

Volkov, A. N., Johnson, R. E., & Tucker, O. J. 2013, FlDy, 48, in press
Volkov, A. N., Tucker, O. J., Erwin, J. T., & Johnson, R. E. 2011c, Supplementary material to the paper by Volkov et al. (2011b) published online at http://dx.doi.org/10.1063/1.3592253
Wagner, W. 1992, JSP, 66, 1011
Watson, A. J., Donahue, T. M., & Walker, J. C. G. 1981, Icar, 48, 150
Yelle, R. V. 2004, Icar, 170, 167
Zahnle, K. J., & Kasting, J. F. 1986, Icar, 68, 462
Zucker, R. D., & Biblarz, O. 2002, Fundamentals of Gas Dynamics (2nd ed.; New Jersey: Wiley)